

NEUROSCIENCE

A biomarker-authenticated model of schizophrenia implicating NPTX2 loss of function

Mei-Fang Xiao^{1†}, Seung-Eon Roh^{1†}, Jiechao Zhou¹, Chun-Che Chien¹, Brendan P. Lucey², Michael T. Craig³, Lindsay N. Hayes¹, Jennifer M. Coughlin⁴, F. Markus Leweke^{5,6}, Min Jia¹, Desheng Xu¹, Weiqiang Zhou⁷, C. Conover Talbot Jr⁸, Don B. Arnold⁹, Melissa Staley⁴, Cindy Jiang⁴, Irving M. Reti⁴, Akira Sawa^{1,4,10,11}, Kenneth A. Pelkey¹², Chris J. McBain¹², Alena Savonenko¹³, Paul F. Worley^{1,14*}

Schizophrenia is a polygenetic disorder whose clinical onset is often associated with behavioral stress. Here, we present a model of disease pathogenesis that builds on our observation that the synaptic immediate early gene NPTX2 is reduced in cerebrospinal fluid of individuals with recent onset schizophrenia. NPTX2 plays an essential role in maintaining excitatory homeostasis by adaptively enhancing circuit inhibition. NPTX2 function requires activity-dependent exocytosis and dynamic shedding at synapses and is coupled to circadian behavior. Behavior-linked NPTX2 trafficking is abolished by mutations that disrupt select activity-dependent plasticity mechanisms of excitatory neurons. Modeling NPTX2 loss of function results in failure of parvalbumin interneurons in their adaptive contribution to behavioral stress, and animals exhibit multiple neuropsychiatric domains. Because the genetics of schizophrenia encompasses diverse proteins that contribute to excitatory synapse plasticity, the identified vulnerability of NPTX2 function can provide a framework for assessing the impact of genetics and the intersection with stress.

INTRODUCTION

Schizophrenia presents in late adolescence or early adulthood with social withdrawal, social cognitive deficits, reduced spontaneous speech, delusions, and hallucinations (1). The diagnosis is based on clinical history and examination, which distinguish it from diseases that exhibit partially overlapping symptoms, including bipolar disorder, schizoaffective disorder, autism, and attention-deficit/hyperactivity disorder (ADHD) (1). Twin studies demonstrated a genetic basis for schizophrenia more than 80 years ago (2), and while human genome sequencing projects reported risk gene “hubs” based on biochemical associations with the *N*-methyl-D-aspartate (NMDA) receptor or *Arc* (3, 4), follow-up studies of individual genes challenged a simple causal association (5). Current studies appear to implicate specific synaptic genes, including NMDA receptor (NMDAR) subunit *GluN2A*,

AMPA receptor *GluA3*, and voltage-dependent calcium (Ca^{2+}) channel (<https://schema.broadinstitute.org/>), as well as C4 complement, which is implicated in developmental synaptic plasticity (6), but specific mutations are uncommon in individuals. A current model proposes that schizophrenia emerges from a combination of polygenic load that may directly or indirectly affect synaptic function and environmental stressors, such as early-life infection or behavioral trauma (7). A successful model of disease needs to integrate genetics with developmental stress and rationalize diverse phenotypes linked to schizophrenia, including altered behavior (1), interneuron function (8), dopamine receptor function (9), NMDA receptor function (10), and a constellation of imaging, electrophysiological, and neurochemical biomarkers (11).

We begin our analysis with the observation that a neuronal immediate early gene (IEG) protein, NPTX2 (neuronal pentraxin 2), is reduced in cerebrospinal fluid (CSF) of individuals with recent onset schizophrenia in two independent cohorts. Because the complex genetics of schizophrenia strongly mitigates against any single gene involvement across all or most individuals, we inferred that the observed reduction of NPTX2 in CSF may represent a common consequence of the diverse genetics or environmental factors that are causal for disease. NPTX2 is dynamically expressed by excitatory pyramidal neurons (PNs) of the cortex and hippocampus in concert with other IEGs, including *Arc* and *Homer1a*, in response to patterned activity that activates postsynaptic NMDA receptors (12). *Arc*, *Homer1a*, and NPTX2 proteins each mediate nonredundant contributions to synaptic plasticity. *Arc* and *Homer1a* act cell-autonomously within the sparse population of PNs that express the IEG program in response to a particular behavioral experience. *Arc* protein binds transmembrane AMPA regulatory protein and other synaptic proteins and promotes their removal from synapses in both Hebbian and non-Hebbian forms of plasticity (13–16). In vivo, *Arc* is required for establishment of new behavior-linked PN ensembles (17, 18). *Homer1a* binds group 1 metabotropic glutamate receptors and

¹Solomon H. Snyder Department of Neuroscience, Johns Hopkins University School of Medicine, Baltimore, MD, USA. ²Department of Neurology, Washington University School of Medicine in St. Louis, St. Louis, MO, USA. ³Institute of Biomedical & Clinical Science, University of Exeter Medical School, Exeter, UK. ⁴Department of Psychiatry and Behavioral Sciences, Johns Hopkins University School of Medicine, Baltimore, MD, USA. ⁵Central Institute of Mental Health, Department of Psychiatry and Psychotherapy, Medical Faculty Mannheim, Heidelberg University, Mannheim, Germany. ⁶Youth Mental Health Team, Brain and Mind Centre, Central Clinical School, Faculty of Medicine and Health, The University of Sydney, Sydney, NSW, Australia. ⁷Department of Biostatistics, Johns Hopkins Bloomberg School of Public Health, Baltimore, MD, USA. ⁸Transcriptomics and Deep Sequencing Core Facility, Johns Hopkins University School of Medicine, Baltimore, MD, USA. ⁹Department of Biology, Section of Molecular and Computational Biology, University of Southern California, Los Angeles, CA, USA. ¹⁰Department of Biomedical Engineering, Johns Hopkins University School of Medicine, Baltimore, MD, USA. ¹¹Department of Mental Health, Johns Hopkins University Bloomberg School of Public Health, Baltimore, MD, USA. ¹²Program in Developmental Neurobiology, Eunice Kennedy-Shriver National Institute of Child Health and Human Development, Bethesda, MD, USA. ¹³Department of Pathology, Johns Hopkins University School of Medicine, Baltimore, MD, USA. ¹⁴Department of Neurology, Johns Hopkins University School of Medicine, Baltimore, MD, USA.

*Corresponding author. Email: pworley@jhmi.edu

†These authors contributed equally to this work.

induces glutamate-independent receptor activity (19) that drives homeostatic scaling and excitatory synapse downscaling during sleep (20, 21). Homer1a also mediates a form of dopamine receptor metaplasticity that conditionally stabilizes potentiated synapses (22). NPTX2, by contrast, acts non-cell autonomously to strengthen excitatory efferents of PNs specifically on parvalbumin interneurons (PVs) (23–25). The time course of NPTX2 protein expression is delayed relative to Arc and Homer1a, peaking 12 hours after a stimulus and remaining elevated for up to 48 hours (26). De novo NPTX2 forms disulfide-linked heteromultimers with cofunctional pentraxins NPTX1 and NPTXR and is transported along axons and exocytosed from presynaptic sites at excitatory synapses on PVs (23, 27). Presynaptic NPTX1/2/R complex binds and clusters postsynaptic AMPA receptors, thereby enhancing synaptic strength and increasing PN drive of inhibitory circuits (23, 25, 26). While NPTX1 and NPTXR are constitutively expressed and broadly present at excitatory synapses on PNs (27, 28), NPTX2 appears to enhance targeting of the complex to presynaptic sites on PVs (23, 25, 29). The NPTX1/2/R complex is later removed from the synapse through enzymatic cleavage of the complex by sheddases acting at the transmembrane domain of NPTXR, and the cleaved, disulfide-linked complex is detectable in CSF (28, 29). Specific mechanisms of presynaptic shedding have not yet been described.

In examining the role of NPTX2 in memory function, we previously determined that NPTX2 is reduced in both CSF and neocortex of individuals with Alzheimer's disease (AD) wherein CSF levels correlate with disease status, cognitive performance, and disease progression (29). NPTX1 and NPTXR were not reduced in neocortex of individuals with AD, indicating that NPTX2 is critical for the process that places the NPTX1/2/R complex in CSF. However, our analysis of NPTX1/2/R in brain of individuals with schizophrenia did not detect a consistent reduction. While there are caveats of sampling, observations suggested that NPTX2 trafficking at the synapse, rather than total expression, might be selectively disrupted in schizophrenia. To examine this hypothesis, we developed a vital reporter of NPTX2 synaptic trafficking by fusing it with the pH-sensitive green fluorescent protein (GFP) superecliptic pHluorin (SEP) (30) and report here activity-dependent synaptic exocytosis and behavior-linked circadian cycling of synaptic NPTX2 in vivo. In mouse brain, NPTX2-SEP appears to be shed during sleep in accord with a role in homeostatic scaling. Behavior-linked trafficking of NPTX2-SEP is absent in *Arc*^{-/-} or *Homer1a*^{-/-} mice, indicating that NPTX2's contribution to circuit homeostasis is vulnerable to genetic mutations that disrupt plasticity of excitatory synapses of PNs. In addition, we found that mice with *Nptx2* deletion exhibit multiple neuropsychiatric domains, and NPTX2 loss of function results in failure of PVs in their adaptive contribution to behavioral stress. In summary, findings identify CSF NPTX2 as a novel biomarker of schizophrenia and support a model in which NPTX2 function is reduced in individuals with schizophrenia and contributes to disease pathogenesis.

RESULTS

NPTX2 is reduced in CSF of human individuals with schizophrenia in two independent cohorts

We analyzed NPTX1/2/R expression in CSF samples from a cohort of individuals with recent onset schizophrenia (within 5 years of first psychotic symptoms) compared with unrelated, age-matched

controls. Patients in this cohort were recruited by the Johns Hopkins Schizophrenia Center, treated with typical and atypical antipsychotics (table S1), and reported previously (31). Western blot revealed coordinate reductions of NPTX1/2/R in CSF of subjects with schizophrenia compared to controls (Fig. 1A and table S2). As anticipated, the estimated molecular weight of CSF NPTXR was reduced compared to NPTXR derived from brain, consistent with proteolytic cleavage upon shedding the NPTX1/2/R complex into the CSF. Within the schizophrenia cohort, CSF NPTX2 inversely correlated with a measure of cognitive function termed ideational fluency (Fig. 1B and table S3). NPTX2 did not correlate with other neurocognitive tests or with clinical parameters of positive or negative symptoms (table S3). We additionally performed an enzyme-linked immunosorbent assay (ELISA) for NPTX2 to provide a more quantitative measure (Fig. 1C). Receiver operating characteristic (ROC) analysis achieved a diagnostic sensitivity of 78.38%, a specificity of 78.05%, and an accuracy of 78.21% (Fig. 1D).

To validate CSF NPTX2 as a biomarker of schizophrenia, we assayed a second independent cohort of individuals with recent onset schizophrenia. This cohort was recruited by the University of Cologne and the Central Institute of Mental Health in Mannheim, Germany, and the individuals were not on medication at the time of CSF collection (32). NPTX1/2/R proteins measured by Western blot were reduced in schizophrenia individuals (fig. S1, A to C). We confirmed reduction of NPTX2 by ELISA (fig. S1A and table S4).

We examined postmortem brain from individuals with schizophrenia. Consistent with a prior report (33), *Nptx2* mRNA was modestly reduced in dorsal lateral prefrontal cortex (DLPFC) comparing schizophrenia and control individuals (fig. S1D and table S5). By contrast, Western blot measures of NPTX2 were not different in the same samples (fig. S1E). mRNA and protein levels of NPTX1 and NPTXR were also not changed in schizophrenia DLPFC (fig. S1, D and E).

NPTX2 synaptic trafficking in mouse neocortex is induced by activity and linked to diurnal cycle

We used adeno-associated virus 2 (AAV2)–calcium/calmodulin-dependent protein kinase II (CaMKII)–NPTX2-SEP to express an NPTX2-pH-sensitive GFP fusion protein that fluoresces upon exocytosis in PNs. NPTX2-SEP puncta imaged in vivo by two-photon microscopy in cortical layers I to III of primary sensory cortex responded to the size and distribution of synapses (Fig. 2, A and B). NPTX2-SEP puncta surrounded PVs identified in PV-Cre mice by AAV-Flex-PSD95.FingR-tdTomato (34) in a pattern similar to reported NPTX2 staining in vivo (35). NPTX2-SEP mimicked the pattern of PSD95.FingR-tdTomato along dendrites of PVs at presumed excitatory synapses. The emission spectrum of NPTX2-SEP in vivo extended into the red channel, making it difficult to assess precise colocalization with synaptic PSD95.FingR-tdTomato (fig. S2A). We speculate this altered spectral property may be due to oxidation, which is known to photoconvert GFP and GCaMP (36). Confocal microscopy with perfused PV-Cre mouse brain injected with AAV-CaMKII-NPTX2-hemagglutinin (HA)-V5 and AAV-Flex-PSD95.FingR-tdTomato further confirmed strong association of NPTX2 signals with PSD95 (postsynaptic density protein 95) of PVs (Fig. 2C).

In mice coinjected with AAV-CaMKII-C1V1-mCherry and AAV-CaMKII-NPTX2-SEP, optogenetic stimulation increased NPTX2-SEP fluorescent puncta number and volume. Increases

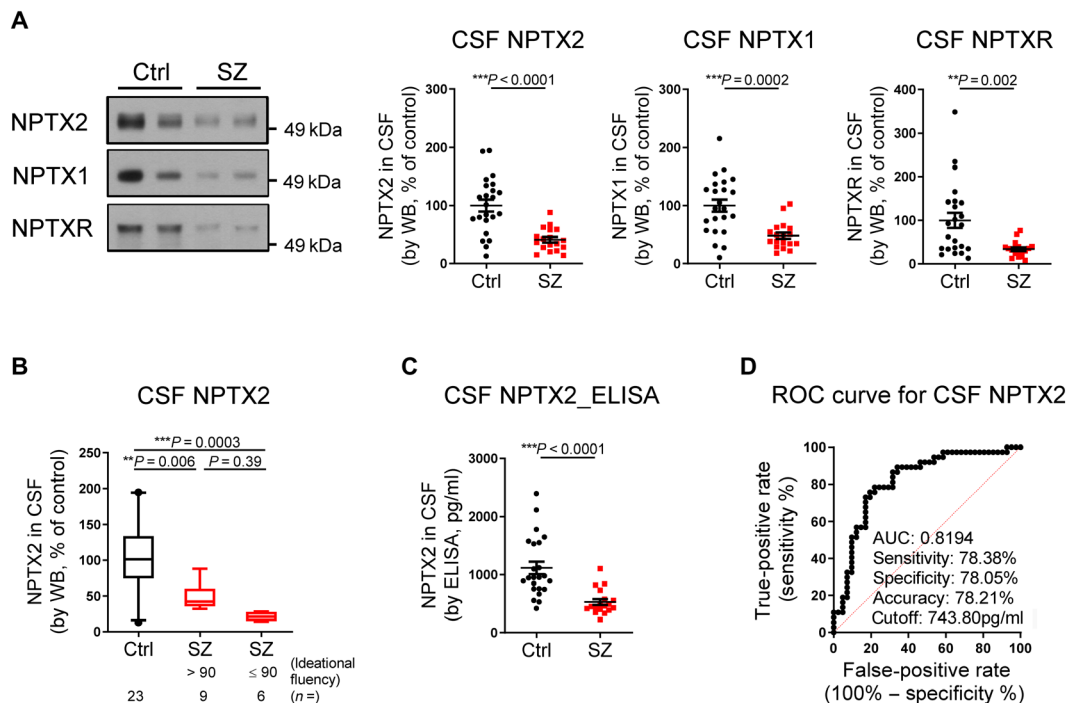


Fig. 1. CSF NPTX levels are reduced in individuals with schizophrenia. (A) Western blot (WB) assays of NPTX2, NPTX1, and NPTXR in lumbar CSF from age-matched healthy controls (Ctrl) and patients with schizophrenia (SZ) with recent onset of psychosis (defined as within 5 years of first psychotic symptoms). NPTX2, NPTX1, and NPTXR levels in CSF are reduced in patients with SZ. Control, $n = 23$; SZ, $n = 18$. ** $P < 0.01$, *** $P < 0.001$, two-tailed t test. (B) CSF NPTX2 levels correlate with ideational fluency in neurocognitive assessment. ** $P < 0.01$, *** $P < 0.001$, one-way analysis of variance (ANOVA). (C) Quantitative ELISA confirms reduction of NPTX2 in CSF from patients with SZ. Control, $n = 23$; SZ, $n = 18$. *** $P < 0.001$, two-tailed t test. (D) ROC curve analysis of CSF NPTX2 as an SZ diagnostic biomarker for distinguishing SZ from control in combined cohorts. Cutoff values were determined by maximizing Youden index value. ROC analysis of NPTX2 indicated its diagnostic accuracy is 78.21%. AUC, area under ROC curve. Control, $n = 41$; SZ, $n = 37$.

reached statistical significance in group data at 2 and 24 hours and returned to baseline after 48 hours (Fig. 2, D to G). In individual animals, NPTX2-SEP puncta number and volume moderately increased within 15 min. This rapid time course was evident for puncta that surrounded the soma of PVs (fig. S2B). Because the CaMKII promoter that drives NPTX2-SEP expression is not sensitive to activity, we infer that increases of the NPTX2-SEP signal represent an increase in exocytosis relative to shedding.

We examined behavior-linked NPTX2-SEP in barrel fields of the primary sensory cortex in male mice. Mice were repeatedly imaged during ~5-min epochs at 4-hour intervals to obtain three-dimensional (3D) time-lapse images over the course of daily activity and sleep. After background and 3D drift correction, 3D images were analyzed with Imaris surface detection function to obtain the number and volume of puncta (fig. S2C). Analysis revealed an increase in NPTX2-SEP puncta number and total volume during their period of behavioral activity (19:00 to 7:00) and a reduction during sleep (light is on at 7:00 and off at 19:00) (Fig. 3, A to C). The maximum amplitude of reduction during sleep was ~50%. This pattern was highly consistent between individual male mice. Selective analysis of puncta that appeared to surround soma showed a similar diurnal change in intensity (fig. S2B). The reduction seen upon “light on” did not require light and was observed when mice were maintained in dark condition during sleep period, indicating a link to their circadian rhythm (fig. S3, A to C).

Next, we examined the effect of sleep deprivation in male mice by gently agitating the mouse cage when mice appeared to initiate

sleep. Imposed sleep deprivation for up to 4 hours prevented the reduction of NPTX2-SEP signal that typically accompanied sleep (Fig. 3, D to F). NPTX2-SEP signal rapidly declined upon subsequent sleep. We conclude that sleep deprivation results in a shift toward increased NPTX2 release by exocytosis or reduced clearance by shedding (or both). We attempted, but failed, to sample mouse CSF in discrete time windows with volumes sufficient to detect native NPTX2 or NPTX2-SEP.

In a complementary study, we examined NPTX2-SEP in mouse visual cortex following monocular deprivation and found a decrease within 24 hours that correlated with “all-or-none” disconnection of ~50% of excitatory synapses from PN to closely proximal PVs in layer 2/3 (37). In this model, overexpression of NPTX2-SEP blocked disconnection while dominant-negative NPTX2 expressed in adult brain reinstated ocular dominance plasticity and was permissive for PN-PV disconnection. These observations provide further evidence in support of a role for NPTX2 in activity-dependent control of PN to PV excitatory connectivity and circuit homeostasis.

CSF NPTX2 levels in healthy human individuals exhibit diurnal changes and increase with voluntary sleep deprivation

To determine whether CSF NPTX2 levels are linked to behavior in human individuals, we examined a cohort of healthy adult individuals in whom CSF was sampled every 2 hours for 36 hours via chronic lumbar catheter (Fig. 4A). The same samples had previously been assayed for A β , tau, and α -synuclein (38–40). A β , tau, and

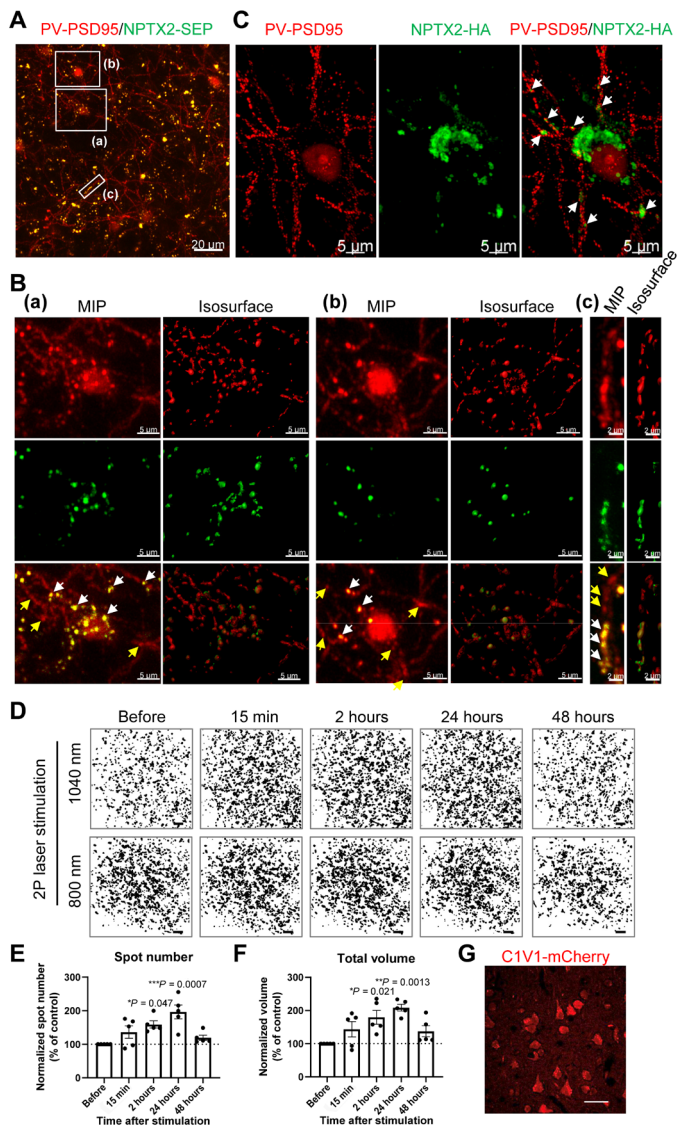


Fig. 2. NPTX2-SEP colocalizes with excitatory synapses on PVs, and its exocytosis is activity dependent in vivo. (A and B) AAV-CaMKII-NPTX2-SEP and AAV-Flex-PSD95.FingR-tdTomato were injected into the sensory cortex of PV-Cre mice. Three weeks later, live animals were imaged with two-photon microscopy under isoflurane anesthesia. Three-dimensional and Imaris isosurface images are shown here. Enlarged images (B) from three boxes in (A) show NPTX2-SEP puncta on soma and processes of PVs. Colocalized or associated signals are indicated by white arrows. Yellow arrows indicate PSD95.FingR-tdTomato signal without NPTX2-SEP. MIP, maximum intensity projection. (C) AAV-CaMKII-NPTX2-HA-V5 and AAV-Flex-PSD95.FingR-tdTomato were injected into the sensory cortex of PV-Cre mice. Perfused brain tissue section was stained with anti-HA for confocal microscopy. Maximum intensity projection of z stack was shown (0.38- μ m interval for 59 stack). NPTX2 accumulation onto PV-PSD95 is indicated by white arrows. (D) Representative Imaris isosurface images of NPTX2-SEP before and after (15 min, 2, 24, and 48 hours) C1V1 (1040 nm) versus control (800 nm) stimulation in S1 barrel field layer 2/3. Maximum intensity projection of 3D images at 80- to 180- μ m depth is shown. Scale bars, 20 μ m. 2P, two-photon. (E and F) Quantification of the spot number (E) and total volume (F). $N = 5$ animals. * $P < 0.05$, ** $P < 0.01$, *** $P < 0.001$, one-way ANOVA with post hoc Tukey's test compared with "Before." (G) Representative image showing the expression of C1V1-mCherry in L2/3 PN. Image was acquired by confocal imaging of frozen tissue section. Scale bar, 20 μ m.

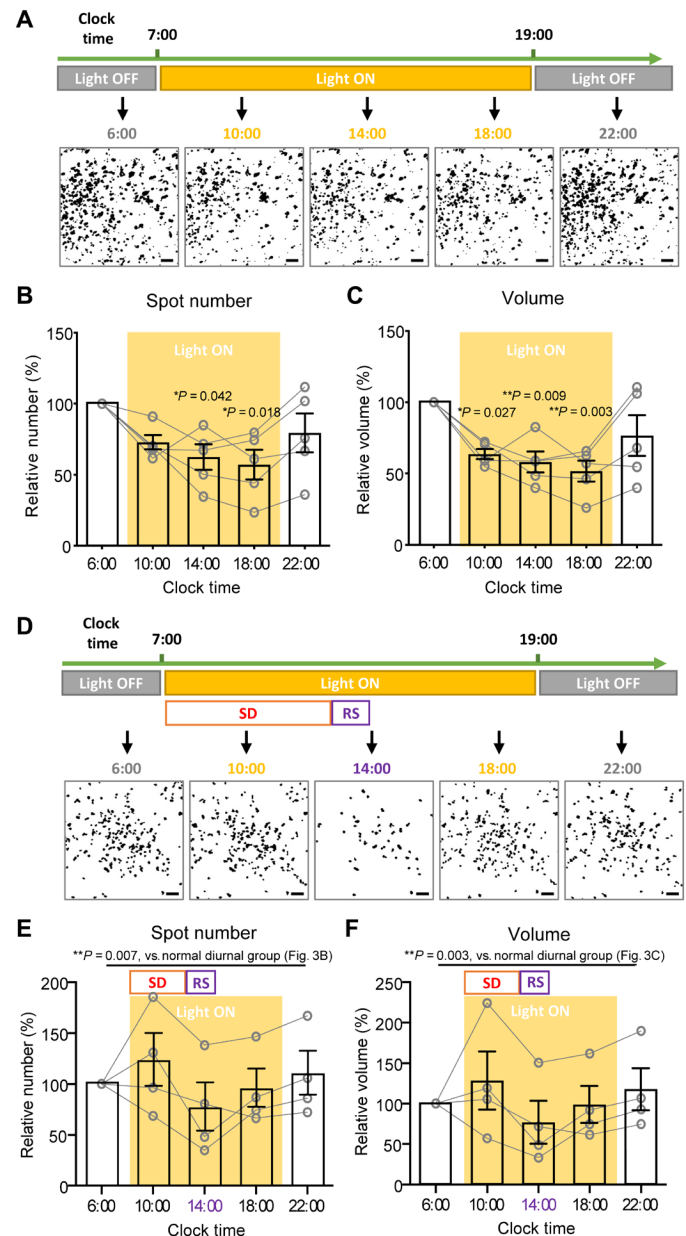


Fig. 3. Extracellular trafficking of NPTX2 is linked to behavioral activity and sleep. (A) The timeline for longitudinal two-photon imaging over the circadian cycle (top) and representative 3D z-stack images from 6:00, 10:00, 14:00, 18:00, and 22:00 (bottom). The light is on at 7:00 and off at 19:00. Maximum intensity projection of Imaris isosurface images of 0 to 180 μ m from the dura of S1 barrel cortex is shown. Scale bar, 20 μ m. (B and C) Quantification of spot number and volume of NPTX2-SEP signals from 3D stack images. $N = 5$ animals. One-way ANOVA and post hoc Tukey's test were performed, and P values were obtained compared to the first time-point data. (D) The imaging schedule of sleep deprivation (SD) by gentle handling for 6 hours (07:00 to 13:00) followed by 1 hour of recovery sleep (RS). Imaris isosurface images for each time point are shown. Scale bar, 30 μ m. (E and F) Quantification of spot number and volume over the cycle. $N = 4$ animals. Two-way ANOVA was performed between normal diurnal cycle group (B and C) and sleep deprivation group (E and F).

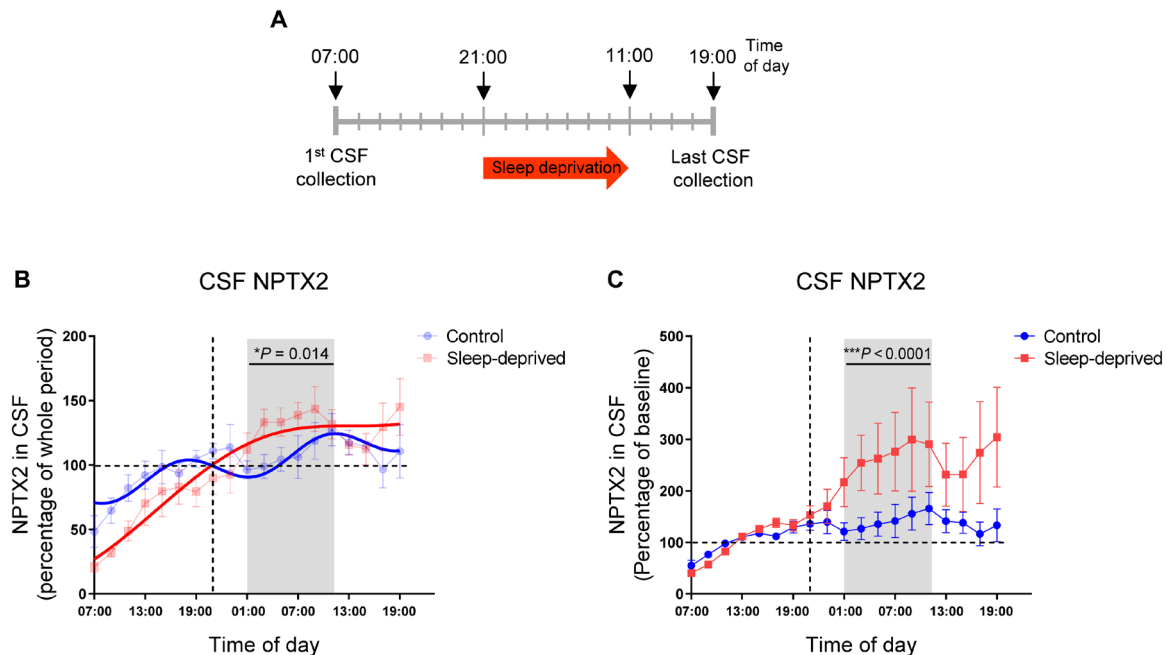


Fig. 4. CSF NPTX2 in healthy human individuals is diurnal and increases with voluntary sleep deprivation. (A) CSF was collected from a cohort of healthy human individuals every 2 hours for 36 hours via an intrathecal lumbar catheter. Sleep deprivation began at 21:00. NPTX2 levels in CSF were determined by ELISA. (B) All NPTX2 concentrations were normalized to the average of the whole period for each participant. Cosinor analysis reveals that CSF NPTX2 has diurnal oscillation in control group (amplitude, 11.28%; period, 17.25; $P = 0.035$). Sleep-deprived group shows different diurnal phase (amplitude, 20.75%; period, 45.75; $P = 0.001$) and increased CSF NPTX2 during the overnight period 01:00 to 11:00. (C) All NPTX2 concentrations were normalized to the average of the baseline 07:00 to 19:00. Sleep deprivation results in a rapid and sustained increase of overnight CSF NPTX2 over the baseline compared with control group. Horizontal dashed line indicates the 100% of baseline, which is the average of hours 07:00 to 19:00 for each individual. Vertical dashed line indicates hour 21:00 when sleep interventions began. Shaded area is the overnight period 01:00 to 11:00 shifted 4 hours to account for CSF transit time from the brain to lumbar catheter. Control, $n = 6$; sleep-deprived, $n = 5$. One-way ANOVA. Data represent means \pm SEM.

α -synuclein are all released with neuronal activity and increase with sleep deprivation because of increased production/release (38–40). As seen in A β and tau analysis, CSF NPTX2 also showed a progressive increase due to the sampling frequency and volume. Cosinor fit analysis, a nonlinear regression model, revealed diurnal oscillation of CSF NPTX2 in control group with an amplitude of 11.28% and a period of 17.25 hours (Fig. 4B). Sleep deprivation resulted in a robust and sustained increase of overnight CSF NPTX2 compared with the control group when normalized to the average of the whole period (Fig. 4B) or to the first 12-hour baseline (Fig. 4C and fig. S4). Corrected for an estimated 4-hour transit time for CSF to move from brain to lumbar thecal space (39, 40), increases in NPTX2 coincided with the onset of sleep deprivation. This increase was not attributable to reduced clearance because other CSF proteins including glial fibrillary acidic protein and neurofilament light chain did not change with sleep deprivation (39). The rapidity of NPTX2 accumulation in CSF during sleep deprivation is consistent with increased release by exocytosis and clearance to the CSF through shedding rather than increased de novo NPTX2 protein generation. We note that human CSF data appear reciprocal to findings in mice where imposed sleep deprivation prevents the normal reduction. This may be related to species differences in the effect of sleep deprivation on exocytosis versus shedding or different consequences of voluntary versus involuntary sleep deprivation.

Behavior-linked NPTX2-SEP synaptic trafficking is dependent on Arc and Homer1a

The delayed time course of NPTX2 expression in PNs (26) and activity and sleep dependence of exocytosis and shedding (Fig. 2) suggested that NPTX2 trafficking might be dependent on plasticity mechanisms required to establish stable ensembles that can sustain reactivation hours after NPTX2 transcriptional induction and protein expression. We noted that Arc is required for network reactivation and for stable behavior-linked excitatory ensembles (17, 18) and therefore imaged NPTX2-SEP in the barrel field of primary sensory cortical neurons of male *Arc*^{-/-} mice. Over the course of the circadian cycle, NPTX2-SEP signal was stable in *Arc*^{-/-} mice without increases or decreases in spot number or total volume of NPTX2-SEP (Fig. 5, A to C). When averaged across six *Arc*^{-/-} mice, there was no change associated with diurnal behavior. Native NPTX1, 2, and R expression in *Arc*^{-/-} were not different from littermate wild-type (WT) mice (fig. S5), suggesting that while activity patterns are sufficient for expression of NPTX2 protein, they do not support its normal behavior-linked trafficking.

Down-regulation of synaptic NPTX2 during sleep parallels the action of Homer1a in mediating downscaling of excitatory synapses of PN (21). The notion that diurnal changes in excitatory synapse strength are balanced by inhibitory circuit modulation is supported by the observation that firing rate does not show a prominent diurnal change (41) despite evidence of diurnal changes in excitatory

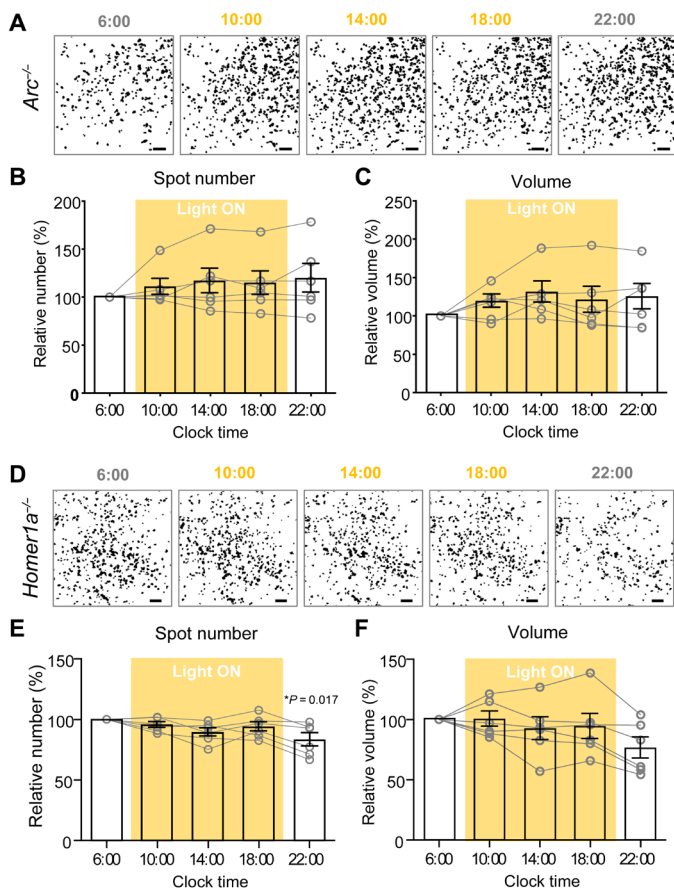


Fig. 5. Diurnal NPTX2-SEP trafficking is abolished in *Arc*^{-/-} and *Homer1a*^{-/-} mice. (A) Representative 3D Z-stack images at 6:00, 10:00, 14:00, 18:00, and 22:00 (bottom) in *Arc*^{-/-} mice, where the light is on at 7:00 and off at 19:00. Maximum intensity projection of Imaris isosurface images of 0 to 180 μm from the dura of S1 barrel cortex is shown. Scale bars, 20 μm . (B and C) Quantification of spot number and volume of NPTX2-SEP signals in from the 3D stack images in (A). $N = 6$ animals. One-way ANOVA identifies no significant difference between time points. (D) Representative 3D Z-stack images at indicated time in *Homer1a*^{-/-} mice, where the light is on at 7:00 and off at 19:00. Maximum intensity projection of Imaris isosurface images of 0 to 180 μm from the dura of S1 barrel cortex is shown. Scale bars, 30 μm . (E and F) Quantification of spot number and volume of NPTX2-SEP signals from the 3D stack images from (D). $N = 6$ animals. One-way ANOVA followed by Tukey's test was performed. * P value compared to the first time point is indicated.

synapse strength (21, 42, 43). To examine the interdependence of NPTX2 synaptic trafficking with excitatory synapse homeostatic scaling, we examined NPTX2-SEP trafficking in *Homer1a*^{-/-} mice. Like in *Arc*^{-/-} mice, NPTX2-SEP present in the barrel field of the primary sensory cortex in *Homer1a*^{-/-} mice failed to show an association with diurnal behavior (Fig. 5, D to F). Moreover, like in *Arc*^{-/-}, native NPTX1, 2, and R protein expressions were not different in *Homer1a*^{-/-} from WT control mice.

Nptx2^{-/-} mice exhibit neuropsychiatric behavioral abnormalities and are vulnerable to social isolation

Arc^{-/-} mice have previously been reported to exhibit multiple neuropsychiatric domains (44). To assess whether NPTX2 loss of function alone can contribute to disease domains, we examined

behavioral phenotypes of *Nptx2*^{-/-} mice. Group-housed *Nptx2*^{-/-} mice are healthy in all parameters of growth and reproduction and perform as well as WT littermate mice in tests of cognition, including acquisition and long-term fear memory (Fig. 6, A and B, and fig. S6A). However, when tested for cued fear memory in a novel context, *Nptx2*^{-/-} mice revealed high secondary fear in the absence of a foot shock (Fig. 6C). As fear memories to context and conditioned stimulus (CS; cue) were similar between *Nptx2*^{-/-} and control mice (Fig. 6, A and B), exaggerated secondary fear conditioning is unlikely due to amplified general fear response. There was no substantial involvement of fear generalization because *Nptx2*^{-/-} and control mice demonstrated similarly low levels of initial freezing when placed in the novel context (Fig. 6C). Accordingly, exaggerated secondary conditioning in *Nptx2*^{-/-} mice is likely due to a failure to reassign or revise the biological value of previously learned CS. This interpretation is in agreement with previously shown effects of dominant-negative NPTX2 on devaluation of contextual stimuli in morphine-induced place preference (45).

Group-housed *Nptx2*^{-/-} mice also showed reduced preference for interaction with social, compared to inanimate, objects (Fig. 6D and fig. S6B). This phenotype did not correlate with anxiety because a measure of anxiety derived from an open-field test explained only 6% of variability in social investigation (fig. S6, C to F). Testing of sensorimotor gating in *Nptx2*^{-/-} mice revealed reduced prepulse inhibition (PPI) of the startle response (Fig. 6E). This deficit coincided with reduced startle amplitude in *Nptx2*^{-/-} mice (fig. S6G); however, deficits in PPI and startle reactivity were not correlated within animals (fig. S6H). Group-housed *Nptx2*^{-/-} mice also demonstrated higher sensitivity to amphetamine-induced locomotor activation than WT littermates (Fig. 6F), while reactivity to the NMDAR antagonist, MK-801, was not different from controls (Fig. 6G, left).

We next examined the effect of stress during adolescence and early adulthood by imposing social isolation at weaning (3-week-old) (46). Socially isolated *Nptx2*^{-/-} mice acquired additional behavioral domains relevant to schizophrenia. Single-housed *Nptx2*^{-/-} mice exhibited increased locomotor activation in response to NMDAR antagonist MK-801 (Fig. 6G, right) and increased novelty-induced activation in multiple environments (Fig. 6, H to M). Social isolation did not alter spatial working memory in *Nptx2*^{-/-} mice tested in a spontaneous alternation protocol in Y maze (Fig. 6N).

Social isolation induces NPTX2-dependent strengthening of PN drive of PV and enhanced PV-mediated inhibition

Social isolation induces down-regulation of multiple IEGs expressed in PNs of WT rodents (47). We examined WT and *Nptx2*^{-/-} mice and confirmed reductions of *Arc*, *Egr1*, *Fos*, and *Homer1a* mRNAs and Arc protein in hippocampus and cortex of single-housed WT mice (Fig. 7A and fig. S7A). Notably, *Nptx2* mRNA and NPTX2 protein were not reduced in single-housed WT mice. By contrast, in *Nptx2*^{-/-} mice IEG mRNAs and Arc protein expression were not down-regulated by single housing, suggesting that IEG down-regulation is dependent on NPTX2.

To further examine adaptations to developmental stress, we performed electrophysiological recordings from PVs in acute hippocampal slices and compared group-housed versus single-housed WT and *Nptx2*^{-/-} mice. In WT mice, patch-clamp recordings from PVs revealed that social isolation increased the AMPA receptor component of the evoked excitatory response relative to the

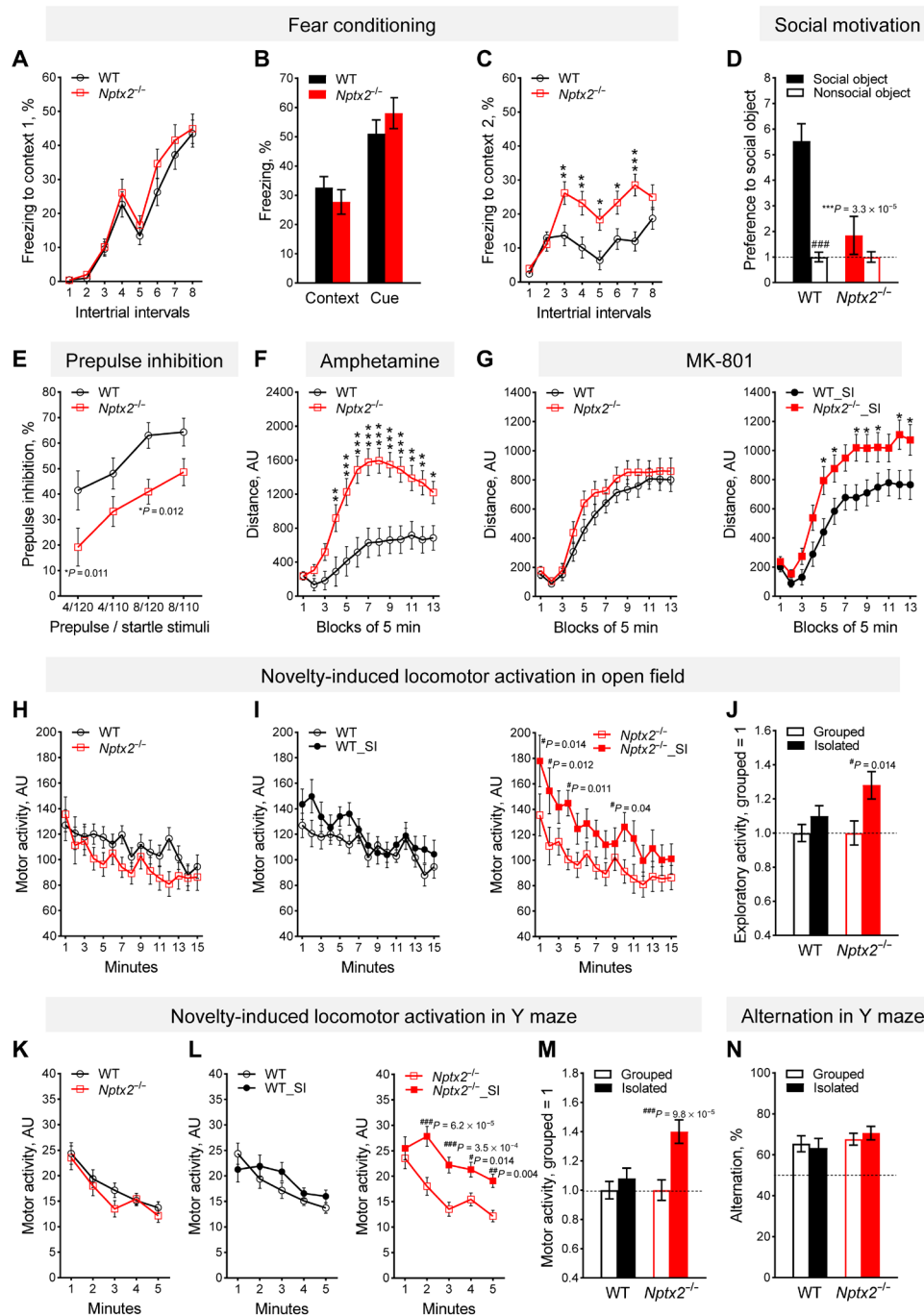


Fig. 6. *Nptx2*^{-/-} mice exhibit neuropsychiatric behavioral deficits, which are exaggerated by postweaning social isolation. (A to C) Group-housed *Nptx2*^{-/-} mice trained in a delayed fear conditioning paradigm reveal normal acquisition of freezing responses to context (A) and long-term memory tested 7 days later (B). (C) Presentation of conditioned stimulus (CS) in a new context resulted in higher levels of secondary contextual fear in *Nptx2*^{-/-} mice compared with WT. *P* values for intertrial intervals 3, 4, 5, 6, and 7 are 0.008, 0.005, 0.01, 0.02, and 0.0005, respectively. (D) Group-housed *Nptx2*^{-/-} mice show deficits in social motivation assessed in a three-chamber test. Preference to social object in *Nptx2*^{-/-} mice was significantly lower than in WT. ****P* = 3.3 × 10⁻⁵, *Nptx2*^{-/-} versus WT; ###*P* = 2.1 × 10⁻⁵, social versus nonsocial. (E) Group-housed *Nptx2*^{-/-} mice show deficits in sensorimotor gating measured by prepulse inhibition of an acoustic startle response. **P* < 0.05, *Nptx2*^{-/-} versus WT. (F) Group-housed *Nptx2*^{-/-} mice exhibit an exaggerated locomotor response to amphetamine [3 mg/kg, intraperitoneally (i.p.)] as tested in the open field. **P* < 0.05, ***P* < 0.01, and ****P* < 0.001, *Nptx2*^{-/-} versus WT. (G) Social isolation (SI) increases locomotor response to MK-801 (0.3 mg/kg, i.p.) in *Nptx2*^{-/-} mice (right), while group-housed *Nptx2*^{-/-} mice are not different than group-housed WT (left). **P* < 0.05, *Nptx2*^{-/-} versus WT. (H to J) Social isolation increases novelty-induced locomotor activation in *Nptx2*^{-/-} mice as tested in open field. #*P* < 0.05, group-housed versus socially isolated. (K to M) Social isolation increases novelty-induced locomotor activation in *Nptx2*^{-/-} mice as tested in Y maze. #*P* < 0.05, ##*P* < 0.01, and ###*P* < 0.001, group-housed versus socially isolated. (N) Social isolation does not alter spatial working memory in *Nptx2*^{-/-} mice tested in a spontaneous alternation protocol in Y maze. Dotted line indicates the chance level (50%). WT, *n* = 10 to 29; *Nptx2*^{-/-}, *n* = 9 to 25; WT_SI, *n* = 12; *Nptx2*^{-/-}_SI, *n* = 10 to 11; least significant difference post hoc test.

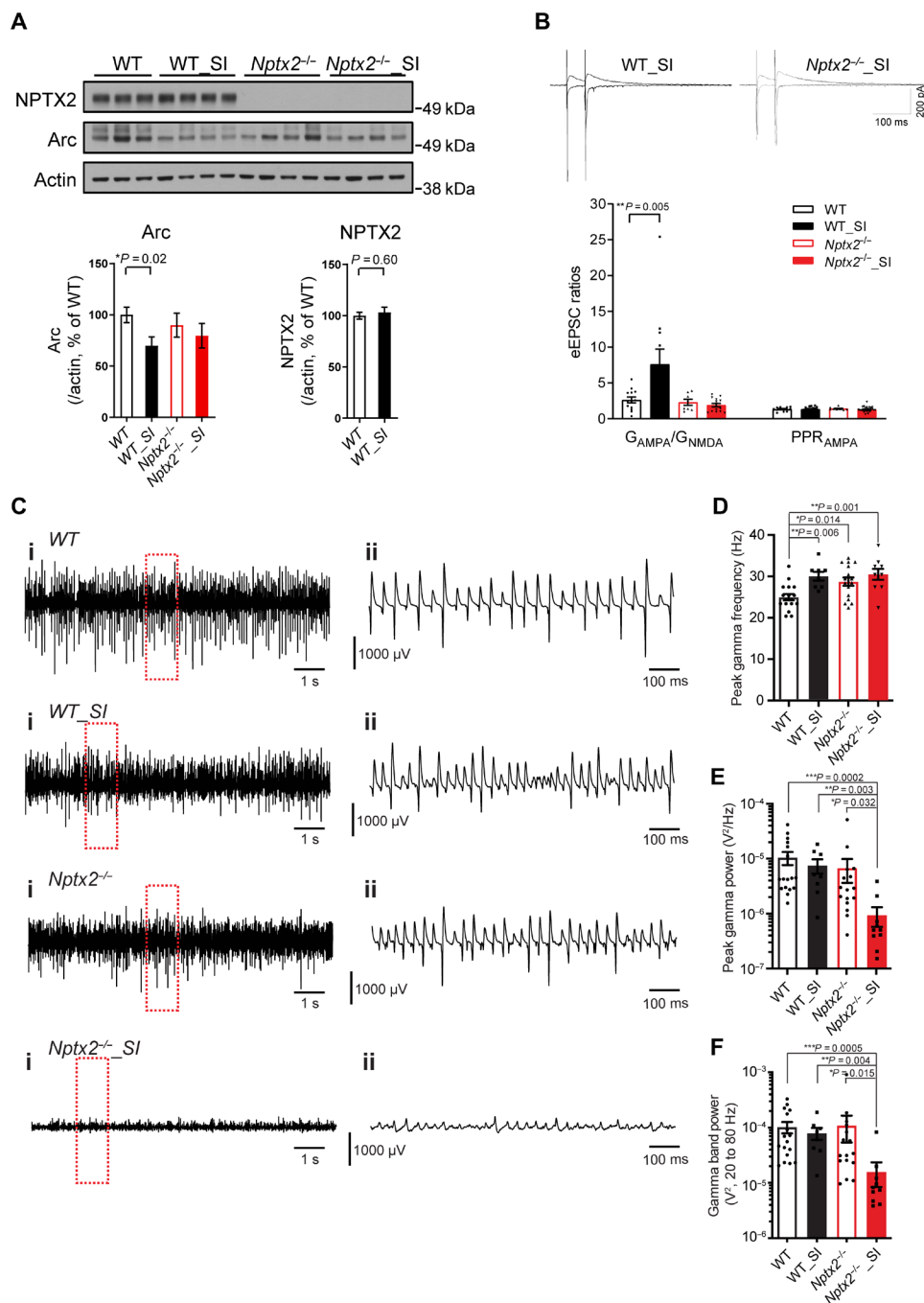


Fig. 7. Postweaning social isolation induces NPTX2-dependent strengthening of excitatory drive of PVs. (A) Western blot shows that Arc protein is down-regulated in cortex of WT mice with social isolation. *N* = 7 to 8 each group. **P* < 0.05, two-tailed *t* test. (B) Averaged AMPA and NMDAR-mediated evoked excitatory postsynaptic currents (eEPSCs) were observed from PVs in hippocampal CA1 of WT and *Nptx2*^{-/-} mice reared in social isolation (upper traces). AMPA-to-NMDA synaptic conductance (G) ratios and paired-pulse ratios (PPRs) of AMPAR-mediated EPSCs are plotted below for all experimental groups. WT, *n* = 13 from 3 mice; WT_Sl, *n* = 11 from 3 mice; *Nptx2*^{-/-}, *n* = 8 from 2 mice; *Nptx2*^{-/-}_Sl, *n* = 15 from 3 mice. (C) Representative traces of persistent gamma oscillations from CA3 in WT, WT_Sl, *Nptx2*^{-/-}, and *Nptx2*^{-/-}_Sl mice. Ten seconds of recording are presented (i) with the red dotted box shown on an expanded time base (ii). (D) The peak frequency of persistent gamma oscillations is slightly, but significantly, higher in all groups of mice versus group-housed WT mice. (E) Socially isolated *Nptx2*^{-/-} display significantly reduced peak power of persistent gamma oscillations. (F) Socially isolated *Nptx2*^{-/-} display significantly reduced gamma-band power of persistent gamma oscillations. WT, *n* = 17; WT_Sl, *n* = 12; *Nptx2*^{-/-}, *n* = 16; *Nptx2*^{-/-}_Sl, *n* = 10. **P* < 0.05, ***P* < 0.01, ****P* < 0.005, Dunn's post hoc multiple comparisons test.

NMDA receptor component. This adaptation to social isolation was lacking in *Nptx2*^{-/-} mice (Fig. 7B). There was no difference in the evoked paired-pulse ratio between genotypes or housing conditions, suggesting that alterations in AMPA/NMDA responses are due to postsynaptic changes at excitatory synapses on PV. These findings are consistent with the known function of NPTX2 mediating homeostatic upscaling of AMPA receptors at excitatory synapses on PVs (23, 25).

In adult hippocampus and cortex, the AMPA receptor GluA4 is preferentially expressed in PV and is essential for fast-spiking properties (25). GluA4 expression is prominently down-regulated in *Nptx2*^{-/-} mice when crossed with either *Nptxr*^{-/-} (25) or amyloid-generating mutations of β -amyloid precursor protein (APP)/PS1 (presenilin 1) (29). However, GluA4 expression in total lysate or in P2 synaptosome fractions was not altered by social isolation in either WT or *Nptx2*^{-/-} mice (fig. S7B). Similarly, there were no changes in total or P2 fraction expression of NMDA receptors GluN1 or GluN2A. Thus, developmental stress and NPTX2-dependent increases in excitatory drive of PV cannot be explained by changes in total glutamate receptor expression.

We next examined a functional assay of PN connectivity with PVs by monitoring carbachol-induced gamma oscillation in field recordings from acute hippocampal slices. Balanced reciprocal connectivity of PN and PV is required to generate rhythmic network activity, especially in the range of ~40 Hz (gamma) observed via the local field potential, and gamma power is proportional to the degree of synchronous firing within hippocampal networks (48). Social isolation did not substantially alter the gamma power or peak frequency in WT mice, and these parameters were not different in group-housed *Nptx2*^{-/-} mice. However, single-housed *Nptx2*^{-/-} mice exhibited a prominent reduction of gamma power (Fig. 7, C to F). Combined findings suggest that effective adaptation to social isolation requires NPTX2-dependent strengthening of the excitatory drive of PV to maintain balanced reciprocal connectivity.

Adaptation to social isolation is associated with changes in PV gene expression that are dependent on NPTX2

To examine the impact of social isolation at rearing on PV gene expression, we performed a RiboTag pull-down analysis of mRNAs expressed in PVs comparing cortex and hippocampus from group-housed versus single-housed WT and littermate *Nptx2*^{-/-} mice. Control experiments confirmed >10-fold enrichment of PV-enriched mRNAs, including parvalbumin and *Gad1*, and depletion of mRNAs that are present in excitatory neurons (*Slc17a7*) or somatostatin interneurons (*Sst*) (Fig. 8A and fig. S8, A and B). A heatmap of biological triplicates (three mice) for each group revealed gene expression changes comparing WT group-housed versus WT single-housed mice yielding 152 differentially expressed genes (DEGs), defined as having *P* values <0.05 and differential log₂ fold changes of >2 SD. By contrast, heatmaps comparing *Nptx2*^{-/-} group-housed mice versus *Nptx2*^{-/-} single-housed mice were more similar (71 DEGs) and notably different than WT single-housed mice (Fig. 8B and fig. S8C). Pathway analysis comparing WT group-housed mice versus WT single-housed mice suggested functions for cognition, diseases of neural excitability, synaptic plasticity, and “first onset paranoid schizophrenia” (fig. S8D). Pathway analysis comparing WT single-housed mice versus *Nptx2*^{-/-} single-housed mice revealed a similar set of pathways (fig. S8D). Analysis of specific biochemical pathways suggested changes in activating

transcription factor 4 (ATF4) signaling (fig. S8E), serine and glycine biosynthesis, and oxidative stress response (Fig. 8, C and D). ATF4 interacts with DISC1 (disrupted in schizophrenia) and is implicated in synaptic dysregulation (49). Select genes identified in the serine and glycine biosynthesis pathway are enriched in PVs, and we confirmed RNA sequencing (RNA-seq) data by quantitative polymerase chain reaction (qPCR) and additionally that changes were specific to PVs versus total RNA (fig. S8, F to I). Glycine biosynthesis converges with oxidative stress response in the generation of glutathione. Indicators of oxidative stress and reduced glutathione are reported in human schizophrenia biospecimens, including brain, CSF, and blood (50). We examined the role of NPTX2 in this adaptation by monitoring the ratio of reduced glutathione to oxidized glutathione disulfide and found an increase in glutathione in single-housed WT mouse brain (compared to group-housed WT) that was absent in single-housed *Nptx2*^{-/-} mice (Fig. 8E). We conclude that *Nptx2*^{-/-} causes multiple neuropsychiatric domains and increases vulnerability to stress during development, in part, by disrupting the ability of PVs to contribute to homeostatic adaptation of inhibitory circuit function.

DISCUSSION

We present a model of schizophrenia that implicates loss of function of NPTX2 in disease pathogenesis. The model builds on three sets of observations. The first provides evidence that levels of NPTX2 are reduced in CSF of individuals with onset of clinically identified schizophrenia within the prior 5 years. The observation that CSF NPTX2 in control individuals shows diurnal changes and rapid increases in response to sleep deprivation supports the notion that CSF NPTX2 reports on a dynamic, behavior-linked processes in human brain. Future studies will need to confirm the observed reduction in additional cohorts of individuals with schizophrenia, assess the association of NPTX2 with other biomarkers of schizophrenia (11), and determine whether CSF NPTX2 can predict clinical onset and whether CSF NPTX2 remains reduced in individuals with chronic schizophrenia. Further analyses of postmortem brain for NPTX2 expression and evidence of loss of function are also warranted.

A second set of observations demonstrates that dynamic trafficking of NPTX2 is normally linked to behavior and is disrupted by genetic mutations that affect synaptic function in PNs. In normal brain, synaptic NPTX2 increases during periods of activity and decreases during periods of sleep. Several lines of evidence suggest that changes of synaptic NPTX2 result in corresponding changes in PN excitatory drive of PVs. Examination of synaptic connectivity in visual cortex of adolescent *Nptx2*^{-/-} mice reveals a selective reduction of layer 2/3 PN connectivity with PVs (24). Moreover, in WT mice, monocular deprivation in adolescent mice results in reduction of connectivity between PN and closely proximal PVs in layer 2/3 with a time course that parallels reduced NPTX2 expression, and NPTX2-SEP overexpression prevents monocular deprivation-induced disconnection of PN-PV (37). Reciprocally, dominant-negative NPTX2 reinstates ocular dominance plasticity in adult brain, suggesting that dynamic changes of NPTX2 are required to establish new functional excitatory circuits (37). It is compelling to suggest that the diurnal changes of synaptic NPTX2, which are comparable in amplitude to those observed with monocular deprivation, similarly contribute to cortical Hebbian and homeostatic plasticity. Continuous

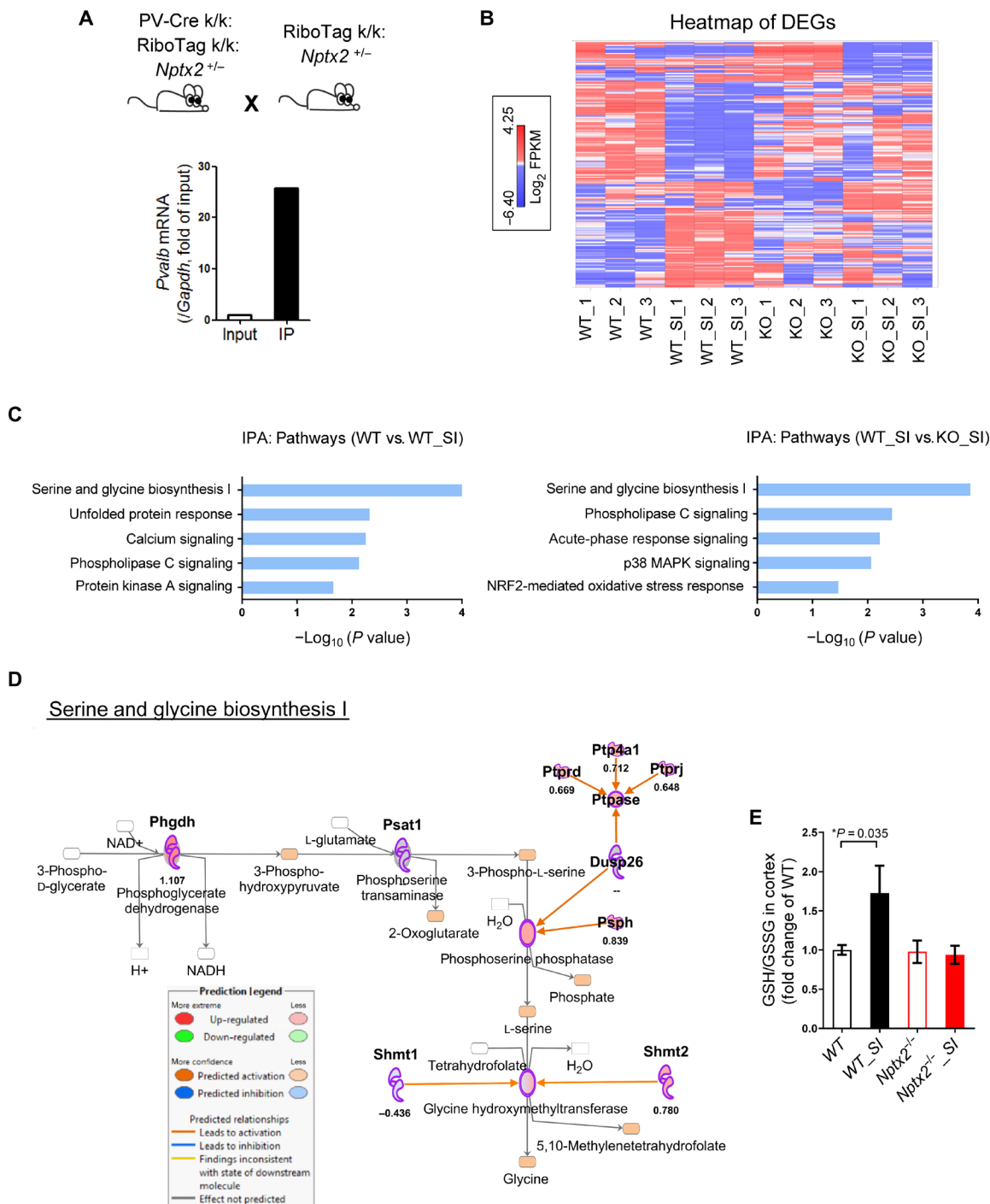


Fig. 8. Adaptation to social isolation is associated with changes in PV gene expression that are dependent on NPTX2. (A) Ribosome-associated mRNA from PVs was extracted by RiboTag pull-down. Quantitative polymerase chain reaction confirmed more than 20-fold enrichment of *Pvalb* mRNA after RiboTag pull-down. PV-Cre k/k; RiboTag k/k; *Nptx2*^{+/-} mice were bred with RiboTag k/k; *Nptx2*^{+/-} mice to generate WT and *Nptx2*^{-/-} mice with PV-Cre k/+; RiboTag k/k. IP, immunoprecipitation. (B) Heatmap of DEGs reveals profound adaptation in PVs of WT mice to postweaning social isolation (WT_SI). PVs in *Nptx2*^{-/-} mice do not show a similar adaptation to social isolation. (C) Dysregulated pathways in socially isolated *Nptx2* KO revealed by Ingenuity Pathway Analysis (IPA). MAPK, mitogen-activated protein kinase; FPKM, fragments per kilobase of transcript per million mapped reads. (D) Ingenuity Pathway Analysis reveals dysregulated serine and glycine biosynthesis pathway in socially isolated *Nptx2* KO in comparison with socially isolated WT. Genes are indicated in bold, and numbers under gene names are the log₂ (fold change) of gene expression (KO_SI versus WT_SI). NAD⁺, nicotinamide adenine dinucleotide; NADH, reduced form of NAD⁺. (E) Postweaning social isolation increases the ratio of reduced glutathione (GSH) to oxidized glutathione (GSSG) in cortex of WT but not *Nptx2*^{-/-} mice. *N* = 5 to 7 per group. **P* < 0.05, two-tailed *t* test. Data represent means ± SEM.

monitoring of network spiking during monocular deprivation in rat revealed immediate onset of reduced PV firing before major changes in PN firing, suggesting that visual stimuli-mediated excitatory drive of PVs is adaptively tuned to balance the overall excitatory input to PNs and thereby establish circuit “criticality” (41, 51).

The role of sleep in regulating synaptic NPTX2 is notable because sleep is disrupted in up to 80% of individuals with schizophrenia (52). Studies including electron microscopy ultrastructure, molecular genetics, and electrophysiological recordings indicate that synapses become stronger during diurnal periods of wake behavior and become weaker during sleep (21, 42, 43). During this cycle, the average firing rate is not significantly different (41), suggesting that changes in excitatory synapses on PNs are balanced by circuit-based inhibition. Consistent with this notion, the decrease of synaptic NPTX2 during sleep is concurrent with Homer1a scaling down of excitatory synapses on PNs (21). The CSF samples from normal human volunteers assayed here for NPTX2 were previously assayed for A β , and demonstrated increases were attributed to increased generation (38). Activity-dependent A β generation is dependent on Arc, which recruits gamma secretase to endosomes that traffic and process APP in the same postsynaptic process that mediates scaling down of synaptic AMPA receptors (53). Thus, CSF A β may represent a biomarker of Arc-dependent homeostatic scaling in normal individuals and, combined with NPTX2, could provide further translational insight into synaptic homeostasis in disease.

Behavior-linked synaptic NPTX2 trafficking is disrupted by mutations that disrupt activity-dependent synaptic plasticity without changing the expression of NPTX2. This finding may rationalize findings of reduced CSF NPTX2 in individuals with schizophrenia without measurable changes in brain NPTX2 protein (Fig. 1). Because NPTX2 synaptic exocytosis is activity dependent, its natural dynamic expression in sparse populations of neurons requires the same neurons that were initially activated to induce *Nptx2* mRNA, and protein expression must be reactivated hours later when NPTX2 protein is expressed and has reached presynaptic sites. Accordingly, we propose a requirement for stable ensemble formation, as ascribed to Arc (17, 18) and as proposed as a role for homeostatic scaling (54) as a basis for proper NPTX2 synaptic trafficking and function. We note that the intensity of the NPTX2-SEP signal in *Arc*^{-/-} and *Homer1a*^{-/-} mice is similar to WT, indicating that exocytosis can occur over the time frame of NPTX2-SEP transgene expression (3 weeks) and that disruption of shedding as normally occurs in sleep may contribute importantly to loss of behavior-linked trafficking.

The third set of observations examines the consequence of NPTX2 loss-of-function screening for neuropsychiatric dimensions. We note that *Arc*^{-/-} mice, with their loss of behavior-linked NPTX2 trafficking, exhibit multiple neuropsychiatric dimensions (17, 18). *Nptx2*^{-/-} results in cortical and hippocampal developmental phenotypes (24, 25), social interaction deficits, and amplified locomotor responses to dopaminergic agents. Yet, performance on many cognitive tasks is preserved, including spatial learning and fear conditioning. *Nptx2*^{-/-} mice exhibit a selective inability to “update” certain memories, which may be relatable to cognitive deficits in presymptomatic individuals (55).

As part of our screen for neuropsychiatric dimensions, we monitored the effect of social isolation stress. Social isolation is strongly associated with psychiatric diseases. Hikikomori (prolonged

social withdrawal) of Japan and mental health issues related to recent social distancing are poignant examples. In rodent models, social isolation engages stress hormones, and aspects of the response can be blocked by glucocorticoid receptor antagonists (46). In WT mice, the response to social isolation involves scaling up of AMPA receptor responses at excitatory synapses on PVs together with reduced IEG mRNA expression in PNs, including *Arc* and *Homer1a* (but not reduced *Nptx2*). This reduction of IEG expression is absent in *Nptx2*^{-/-} brain, consistent with its action to increase circuit inhibition. The prominent change in PV gene expression noted in RiboTag pull-down experiments is indicative of the complexity of adaptations that normally occur as part of the response to social isolation and presumably underlie changes in synaptic strength and in metabolic pathways including serine/glycine biosynthesis. Enhanced glutathione levels are part of the normal homeostatic response and represent another domain relatable to schizophrenia (50).

NPTX2-dependent adaptation of PVs is required for hippocampal circuits to maintain normal gamma power and rhythmicity in response to social isolation. Gamma oscillation and ensemble synchrony are important for long-range synaptic connectivity, sensory cortex timing discrimination, and episodic memory (48), domains that are consistently disrupted in schizophrenia. In *Nptx2*^{-/-} mice, social isolation induces an enhanced locomotor response to the use-dependent NMDA receptor antagonist, MK-801. This phenotype may be interpreted to represent NMDAR hypofunction, and this has been a target of therapeutics development for schizophrenia (10). Alternatively, failure of AMPA receptor scaling on PVs means that NMDA receptors contribute a relatively larger role as mediators of synaptic drive, and consequently, behaviors may be more affected by use-dependent antagonists. Thus, NMDA receptor function may appear reduced in schizophrenia as a consequence of NPTX2 loss of function, independent of mutations of the NMDAR.

In summary, the present model of schizophrenia encompasses a broad range of behavioral, neuropharmacological, electrophysiological, biochemical, and molecular hallmarks of schizophrenia, with the unifying concept that NPTX2 function is required for excitatory circuit function and is uniquely vulnerable to failure because of its delayed time of action and requirement for specific patterns of activity for its normal synaptic trafficking. Our model predicts that diverse genetic loads that increase risk for schizophrenia will share a common end point in disrupting NPTX2 function. The availability of an in vivo reporter and a translatable biomarker provides an opportunity to further refine our understanding of schizophrenia.

MATERIALS AND METHODS

Mice

Nptx2^{-/-} mice in congenic C57BL/6J background were obtained from M. Perrin’s laboratory. *Nptx2*^{-/-} mice in outbred CF1 background were obtained from I.M.R.’s laboratory. Upon weaning, WT and *Nptx2*^{-/-} mice were either group-housed or single-housed at weaning for at least 4 weeks before experiments. *PV-Cre* mice (stock no: 017320), *tdTomato* reporter mice (stock no: 007914), and *RiboTag* mice (stock no: 029977) were purchased from the Jackson Laboratory. All mice had free access to water and food and were housed with a 12 hour-12 hour light-dark cycle. All procedures involving animals were under the guidelines of the Johns Hopkins University Institutional Animal Care and Use Committee.

Antibodies

Rabbit anti-NPTX1, rabbit anti-NPTX2, mouse anti-NPTX2, and mouse anti-Arc were described previously (29, 53). All other antibodies are from commercial companies. Sheep anti-NPTXR is from R&D Systems [catalog number: AF4414; research resource identifier (RRID): AB_2153869]; mouse anti-PSD95 is from Thermo Fisher Scientific (catalog number: MA1-046; RRID: AB_2092361); mouse anti-GluN1 is from Millipore (catalog number: 05-432; RRID: AB_390129); rabbit anti-GluN2A is from Sigma-Aldrich (catalog number: G9038; RRID: AB_259980); rabbit anti-GluA4 is from Millipore (catalog number: AB1508; RRID: AB_90711); rabbit anti-HA for Western blot is from eBioscience (catalog number: 14-6756-81; RRID: AB_468301); mouse anti-HA for RiboTag pulldown is from Sigma-Aldrich (catalog number: H3663; RRID: AB_262051); mouse anti-actin is from Sigma-Aldrich (catalog number: A2228; RRID: AB_476697); ECLTM (enhanced chemiluminescence) anti-mouse immunoglobulin G (IgG) horseradish peroxidase (HRP) is from GE Healthcare (catalog number: NA931V); ECLTM anti-rabbit IgG HRP is from GE Healthcare (catalog number: NA934V); donkey anti-sheep IgG HRP is from Santa Cruz Biotechnology (catalog number: sc-2473; RRID: AB_641190); and mouse anti-HA is from Santa Cruz Biotechnology (catalog number: sc7392; RRID: AB_627809).

Human postmortem brain

Human brain tissue of schizophrenia and healthy control were obtained from D. Weinberger at Lieber Institute for Brain Development, Johns Hopkins Medical Campus. For Western blot analysis, brain samples were lysed in radioimmunoprecipitation assay (RIPA) buffer [1% Triton, 0.5% Na-deoxycholate, 0.1% SDS, 50 mM NaF, 10 mM Na₄P₂O₇, 2 mM Na₃VO₄, and protease inhibitor cocktail in phosphate-buffered saline (pH 7.4) at a dilution factor 1:50].

Human CSF

Schizophrenia CSF

Human CSF samples were collected from patients with psychosis and healthy controls from two distinct cohorts. One cohort was from patients with recent onset of psychosis (defined as within 5 years of first psychotic symptoms), who were recruited from the Johns Hopkins Medical Institutions and surrounding hospitals from the Greater Baltimore area. Participants in this cohort completed a 2-hour battery of neuropsychological tests to assess cognitive function, as previously described (31). Another cohort was from antipsychotic-naïve patients with schizophrenia, who were recruited from the University of Cologne and the Central Institute of Mental Health in Mannheim, Germany. All participants were given informed consent before taking part in the study.

Sleep intervention CSF

Seven participants with normal cognitive function were recruited from both longitudinal studies at the Knight Alzheimer Disease Research Center and a research volunteer registry at Washington University with written informed consent (38). Participants were randomized to two groups, including control group with normal sleep and sleep-deprived group. Starting at 7:00, CSF samples were collected every 2 hours for 36 hours (from 7:00 to 19:00 the next day) via an intrathecal lumbar catheter. Sleep intervention starts at 21:00.

Human CSF samples were dissolved with SDS loading buffer, and 12 μ l of CSF were loaded to SDS-polyacrylamide gel electrophoresis (SDS-PAGE) and subsequent Western blot. NPTX2 protein levels in CSF were further quantitated by ELISA described

previously. All CSF samples were frozen at -80°C at collection and thawed no more than twice before measurement. Clinic information was blinded during experiment. Two different graphs were presented where values were normalized in two ways: normalized with average from all time points (Fig. 4B) or average from the first 12 hours as baseline (Fig. 4C).

Western blot

Brain tissue were lysed with RIPA buffer. Protein extracts were separated by 4 to 12% SDS-PAGE, transferred to polyvinylidene difluoride membranes, blocked with 5% nonfat milk, and then probed with primary antibodies for overnight at 4°C . After washes with TBST (tris-buffered saline with 0.1% Tween 20), membranes were incubated with HRP-conjugated secondary antibodies for 1 hour at room temperature. Immunoreactive bands were visualized by the enhanced chemiluminescent substrate (Pierce) on x-ray film and quantified using the image software TINA (www.tina-vision.net). PSD95 were used as loading controls. Proteins migrating similarly in SDS-PAGE gel were assayed on different blots without stripping.

Crude synaptosome preparation

Mouse cortex was homogenized in homogenization buffer [5 mM tris-HCl, 0.32 M sucrose, 1 mM MgCl₂, 1 mM CaCl₂, and 1 mM NaHCO₃ plus cComplete EDTA-free protease inhibitor mixture (pH 7.5)] and centrifuged at 1000g for 10 min at 4°C to pellet nuclei and mitochondria (P1 fraction). The resulting supernatant was centrifuged at 16,000g for 20 min at 4°C to pellet crude synaptosome (P2 fraction). The P2 pellet was then resuspended in homogenization buffer and centrifuged at 16,000g for 20 min again to pellet washed crude synaptosome (P2' fraction). Crude synaptosome was resuspended in RIPA buffer, and the protein concentration was determined by bicinchoninic acid assay.

Design of pAAV-CAG-DIO-PSD95.FingR-tdTomato-IL2RGZF (AAV Flex PSD95.FingR)

PSD95.FingR (34), a recombinant, antibody-like protein based on the 110FNIII domain of human fibronectin, was cloned into an AAV vector that expresses genes in a Cre-dependent manner with a double-floxed inverted open reading frame (DIO). PSD95.FingR was fused to tdTomato and to the interleukin-2 receptor subunit gamma (IL2RG) zinc finger transcription factor (ZF) that binds to a 12-nt DNA-binding site (ZFBS) (56). Expression was driven by a β -actin (CAG) promoter. The binding site for the ZF was situated immediately downstream of the TATA box before the transcription start site. Unbound FingR-ZF binds to the ZFBS, inhibiting transcription and reducing background. The woodchuck hepatitis virus posttranscriptional regulatory element was added before the poly A sequence to increase expression. To drive specific expression of PSD95.FingR-tdTomato in PVs, AAV-CAG-DIO-PSD95.FingR-tdTomato-IL2RGZF virus was injected into the brain of PV-Cre mice.

Two-photon microscopy Craniotomy

All experimental procedures were approved by the Johns Hopkins University Institutional Animal Care and Use Committee and performed according to the National Institutes of Health (NIH) guidelines. Cranial windows were created over the barrel field of primary sensory cortex (center position: 3 mm lateral and 1 mm posterior from the bregma) in 7- to 12-week-old WT C57BL/6J,

Arc^{-/-}, or *Homer1a*^{-/-} mice. Anesthesia was induced with 3 to 5% of isoflurane and maintained with 1.2 to 1.5% during surgical procedures on a stereotaxic frame (Kopf, CA). Before the first incision, dexamethasone (0.2 mg/kg) and meloxicam (20 mg/kg) were subcutaneously injected to prevent the edema and related inflammation. After removal of the skin, the custom-made metal head bar was attached using the dental cement Superbond (Sun Medical, Japan). Craniotomy (2 mm by 2 mm) was made with No.11 surgical blade, and AAV9-CaMKIIa-NPTX2-SEP (~10¹² genome copies) was injected at three to four sites in a depth of 200 to 300 μm using pulled glass pipette (Narishge, Japan) and Nanoject (Drummond Scientific Company, PA) at a rate of 5 nl/s. The window was secured with the glass coverslip with cyanoacrylate glue Vetbond (3M, MN), and the animals were recovered for about 2 weeks before two-photon imaging.

Optogenetics

Optogenetic stimulation was carried out to test whether direct neuronal activation results in secretion of NPTX2 *in vivo*. To avoid spectral overlapping with NPTX2-SEP, we used a red-shifted opsin C1V1. AAV-CaMKII-C1V1-mCherry was injected along with AAV-CaMKII-NPTX2-SEP over S1 barrel field. Fifteen to 20 days later, C1V1 was stimulated with 1040 nm of Ti:Sapphire two-photon laser (MaiTai, Spectra-physic), which was 818 mW at layer 2/3. For stimulation, scanning (pixel dwell time, 2.8 μs) was alternated between depths of 120 μm (1 s) and 140 μm (1 s) for 10 min (0.5 Hz). To make sure that there are no heat-induced artifacts, control stimulation was performed with 800-nm wavelength, which does not stimulate C1V1 at 818 mW.

In vivo two-photon awake NPTX2-SEP imaging over normal light-dark cycle, sleep deprivation, and dark-dark cycle

Confocal microscopy was performed with a laser scanning microscope (Olympus, Japan) equipped with an ultrasensitive GaAsP detector (Hamamatsu, Japan) and a galvanometer scanner (Thorlabs, NJ). Two-photon excitation was carried out by ultrafast Ti:Sapphire laser Mai Tai eHP DeepSee (Spectra-Physics, CA), operating the wavelength at 920 nm for visualizing NPTX2-SEP with a GFP filter using a 20× objective XLUMPLFL20XW (Olympus, Japan). Hardware operation and image acquisition were performed with PrairieView software (Bruker, MA).

Eleven to 13 days after surgery, mice were handled for 10 to 15 min and acclimated to the imaging setup for 15 to 30 min by fixing their head bars to the custom-made head fixation apparatus and imaging platform. During the habituation, the blood vessel mapping is performed for a whole window. Blood vessels are images by epifluorescence imaging with 605-nm light-emitting diode excitation (Thorlabs, NJ). The 3D z-stack images were acquired where the expression exists around day 14. Resolution images (512 by 512 pixels) with eight averages were acquired from 0 to 180 μm from dura in an interval of 5 μm (total 37 image stacks). Because of the poor z resolution of two-photon excitation, the image quality between 2- and 5-μm intervals was not very different. Using the blood vessel morphology as a reference, the images were acquired in the same location with the same imaging parameters for longitudinal study during the imaging period: 6, 10, 14, 16, and 20 clock time (CT), where light is on and off at 7 and 19 CT, respectively. For sleep deprivation, we performed gentle handling by gently tapping or agitating the cages whenever the mice were going to fall asleep. Sleep deprivation was performed for 6 hours followed by 1-hour recovery sleep, and each effect on NPTX2 secretion was assessed.

For the dark-dark cycle experiment, the mice were kept in a light-proof chamber that is ventilated during whole imaging sessions.

NPTX2-SEP spot 3D analysis and statistics

All 3D z-stack time-series (4D) images were preprocessed with ImageJ (FIJI) and further analyzed with Imaris software (Bitplane, Zurich, Switzerland). Each set of 3D z-stack images was concatenated to generate time-lapse 3D images, background-corrected by “bleach correction” plug-in using histogram-matching algorithm, and 3D drift-corrected by “Correct 3D drift” algorithm (57) (FIJI). The xyz-corrected portion of the processed 4D images were selected and subjected to NPTX2-SEP spot analysis with Imaris software. The NPTX2-SEP spots were detected with “surface detection” function, the diameter of the largest sphere being 2.5 μm, and the number of spots and volume of each spot were exported. The “total volume” used in this study is defined by the sum of volume of all NPTX2-SEP spots. The spot number and the total volume were normalized with the first time-point data and subjected to one-way analysis of variance (ANOVA) with post hoc Tukey’s test where indicated (GraphPad Prism).

Tissue staining and confocal microscopy

For confocal microscopy of NPTX2 and PV-IN PSD95 colocalization, AAV2-CaMKII-NPTX2-HA-V5 was injected along with AAV-CAG-DIO-PSD95.FingR-tdTomato-IL2RGZF into PV-Cre mice. Perfused brain was sectioned by 20 μm and stained with anti-HA antibody. Images were captured using a laser-scanning confocal microscope (LSM 880, Zeiss) with 100× lens.

Behavioral testing

All procedures involving animals were under the guidelines of Johns Hopkins University Institutional Animal Care and Use Committee. Male *Nptx2*^{-/-} mice and their WT littermates on a C57BL/6J strain background were used in all but fear conditioning testing. Male *Nptx2*^{-/-} mice and their WT littermates on CF1 strain background were used for fear conditioning.

For the part of the study that used social isolation paradigm, the cohorts of littermates were randomly divided into group- (three to four animals) and single-housed subgroups. Single housing was initiated shortly after weaning. Behavioral testing started at least 60 days after the initiation of social isolation.

All testing was performed in isolated behavior rooms at 21 to 22°C. Mice were handled daily for 3 days before start of behavioral testing. Testing was conducted during the light phase of circadian cycle in cohorts of 10 to 15 mice blindly balanced by pseudo-genotype. Before each test, mice were moved to the testing room and allowed to habituate to the new location for at least 1 hour before behavioral testing. Behavioral performances in the open field, Y maze, and social motivation tests were recorded by a computer-based video tracking system (ANY-maze, Stoelting Co., IL). PPI of acoustic startle reaction (ASR) was conducted in a startle soundproof chamber (model SR-LAB, San-Diego Instruments, CA).

Novelty- and drug-induced locomotor activation in open field

Mouse was placed in an open-field arena made of white plastic (38 cm by 38 cm by 25 cm), and each animal performed one daily trial. The trial began with the mouse being released near the wall of a novel open field and lasted for 15 min to measure the novelty-induced motor activity. For measurement of drug-induced locomotor activity, mouse was first placed in the open field for 45 min for habituation trial. After habituation, drugs of indicated dosage were

administered intraperitoneally, and the mouse was placed back to the open field for another 65 min. Following each trial, the fields were cleaned with a dilute alcohol solution and dried with a paper towel. Activity measures included distance traveled, percent time spent in the central area of a field, and percent time spent in active exploration (episodes of movement ≥ 5 cm/s).

Novelty-induced locomotor activation and spontaneous alternation task in Y maze

Testing was carried out on a Y-shaped maze with each arm measuring 8 cm by 53 cm. Mice were placed into the end of one arm and allowed to explore freely for 5 min. The sequence of arm entries and locomotor activity were recorded using ANY-maze software (Stoelting Co., IL). The spontaneous alternation behavior was calculated as the number of trials containing entries into all three arms divided by the maximum possible alternations. Following each trial, the Y maze was cleaned with a 30% alcohol solution and dried with a paper towel.

Social motivation task

Social motivation task was carried out in a three-chamber test [PMID (PubMed identifier): 15344922]. A stimulus animal (23- to 28-day-old male mouse on C57BL6/J background) was placed in an air-transparent enclosure on one side of the apparatus, and an empty enclosure was placed on the other side. The testing animal was allowed to habituate to the three-chamber apparatus, with both enclosures being empty for 10 min. After the habituation, the animal was removed into the waiting cage, and the apparatus and enclosures were thoroughly cleaned with 30% alcohol. For the next trial, the testing animal was placed in the apparatus with a social stimulus present on one of the sides. The time investigating each enclosure and number of entries into each chamber were automatically recorded using the ANY-maze software.

Prepulse inhibition

PPI was tested as described before (PMID: 18385378). During a 6-min acclimation period, the mouse was exposed to a background noise of 63 dB, which continued throughout the session. The subject was then exposed to three 25-ms startle pulses of 120-dB white noise to determine the initial level of ASR. The subject then received six blocks of eight trials each to measure the PPI. Each block of trials consisted of six different trial types presented pseudo-randomly across blocks: startle pulse of 120 dB (two trials); startle pulse of 110 dB (two trials); and four different prepulse trials followed by the startle pulse (one trial for each of the prepulse and startle intensities). The prepulses were 25-ms weak stimuli of white noise with intensities of 4 or 8 dB above the background noise. The time interval between the prepulse offset and the startle pulse onset was 75 ms. Trials were presented at a variable-interval schedule of 20 to 40 s. The maximum amplitude and the latency of the startle reaction were recorded for every trial. The average value for every type of trial across six blocks was used for the statistical analysis. The measures of ASR amplitude to startle pulses of 120 and 110 dB in trials without prepulses were used to characterize the reactivity to acoustic stimuli. PPI was characterized as a percentage of ASR inhibition induced by each prepulse intensity and was calculated as $[100 \times (\text{Startle amplitude in the startle alone trial} - \text{Startle amplitude in the prepulse trial}) / \text{Startle amplitude in the startle alone trial}]$.

Delayed fear conditioning

Delayed fear conditioning is a subtype of classical (Pavlovian) conditioning in which a subject learns to associate a novel context and a neutral CS with an aversive unconditioned stimulus (US). As

a result of the training, previously neutral stimuli become associated with danger and elicit an unconditioned fear response, freezing, in the absence of US (PMID: 11520922). Mouse training chamber (Stoelting Co., Wood Dale, IL) was used as described in (58) (PMID: 23764200). Testing protocol and data collection were automated by ANY-Maze 6.06 software (Stoelting Co., Wood Dale, IL). A mouse was placed in the training chamber with context 1 (black-and-white contrast walls; lights in the chamber, 2.0 visible +0.0 infrared; background noise, 70 dB). After 120 s of habituation, a CS was presented (a 15-s-long 85-dB 600-Hz tone) and coterminated with a mild footshock (US, 2-s long, 0.6 mA). The CS-US pairings were presented with a 120-s-long intertrial interval for a total of six pairings. Freezing duration was measured automatically throughout training with minimum freezing duration = 1000 ms and On/Off threshold = 30/40. To characterize a motor reaction to the US, raw movement scores were used as a number of pixels displaced per second. Training chamber was cleaned thoroughly with a 30% ethanol solution after each mouse.

Fear memory to context was tested 6 days after the fear acquisition session. Mice were placed in the same fear conditioning box (context 1) for 5 min. No CS or US was presented. All other parameters were identical to the fear acquisition training session. Twenty-four hours after testing for contextual fear memory, mice were placed in a novel 25 cm by 25 cm by 38 cm box with white walls and a solid floor (context 2). Fresh bedding was placed on the floor of the box. Mice were allowed to explore the chamber for 120 s, after which the CS was presented for 15 s. This was repeated for a total of six times for each animal to mimic the protocol from the training session. US was not presented. Freezing response during intertrial intervals and each presentation of the CS was analyzed by Any-Maze 6.03 software (Stoelting Co., Wood Dale, IL).

Statistics

The statistics were carried on by using Statistica 13.3 (TIBCO Software Inc., CA) and a minimal level of significance $P < 0.05$. A two- or three-way mixed-design ANOVA was used for most of the behavioral experiments, followed by Fisher's least significant difference post hoc test for significant main effects/interactions. The effects of genotype and/or social isolation were treated as main effects, whereas effects of time periods (blocks of trials or minutes), type of trials (startle or prepulse intensity), or type of object (social versus nonsocial) were treated as repeated measures. All interactions were set as orthogonal. Correlations between different behavioral measures were assessed using Pearson correlations (R) after confirmation of nonviolation for normal distribution. Coefficient of determination (R^2) was calculated to characterize percent of variability explained by correlations. Numbers of cases per group (n) are indicated in the figure legends. All error bars represent SEM. Details of statistical analyses for each panel of main and supplementary figures are presented in Supplementary Materials.

Slice electrophysiology

Slice preparation

WT and *Nptx2*^{-/-} mice that had been maintained in social housing or single housing after weaning for at least 4 weeks were anesthetized with isoflurane and then decapitated. The brain was dissected out in ice-cold sucrose-substituted artificial CSF (SSaCSF) containing the following: 90 mM sucrose, 80 mM NaCl, 3.5 mM KCl, 24 mM NaHCO₃, 1.25 mM NaH₂PO₄, 4.5 mM MgCl, 0.5 mM CaCl₂, and 10 mM glucose, saturated with 95% O₂ and 5% CO₂. Transverse

midventral hippocampal slices (300 μm) were cut using a VT-1200S vibratome (Leica Microsystems) and incubated submerged in SSaCSF at 32° to 34°C for 30 to 40 min and then maintained at room temperature in SSaCSF until use.

Whole-cell slice electrophysiology

For patch-clamp recordings following recovery, slices were transferred to an upright microscope (Zeiss Axioskop) and perfused at 2 to 3 ml/min (32° to 34°C) with aCSF composed of 130 mM NaCl, 3.5 mM KCl, 24 mM NaHCO₃, 1.25 mM NaH₂PO₄, 1.5 mM MgCl₂, 2.5 mM CaCl₂, and 10 mM glucose, saturated with 95% O₂ and 5% CO₂. Individual fluorescently reported PV cells in CA1 were visualized with a 40 \times objective using fluorescence and infrared-differential interference contrast video microscopy. Electrodes were pulled from borosilicate glass (World Precision Instruments) to a resistance of 3 to 5 millionohm using a vertical pipette puller (Narishige, PP-830) and filled with internal solution containing 130 mM Cs-methaneSO₄, 5 mM CsCl, 10 mM Hepes, 3 mM MgCl₂, 2 mM Na₂ adenosine triphosphate, 0.3 mM Na guanosine 5'-triphosphate, 0.6 mM EGTA, and 2 mM Qx-314 10 1,2-bis(2-aminophenoxy)ethane-*N,N,N',N'*-tetraacetic acid and supplemented with 0.2% biocytin. Whole-cell patch-clamp recordings were made using a Multiclamp 700A amplifier (Molecular Devices), and signals were digitized at 20 kHz (Digidata 1322A, filtered at 3 kHz) for collection on a PC equipped with pClamp 9.2 or 10.4 software (Molecular Devices). Uncompensated series resistance ranged from 10 to 20 millionohm and was monitored continuously throughout recordings with -5-mV voltage steps. Excitatory synaptic transmission was pharmacologically isolated by supplementing aCSF with 50 μM picrotoxin, 10 μM bicuculline, and 2 μM CGP 55845. Synaptic events were evoked by low-intensity stimulation (150 μs /10 to 30 μA) via a constant current isolation unit (A360, WPI) connected to a patch electrode filled with oxygenated aCSF. AMPAR-mediated events were recorded at a holding potential of -70 mV and then blocked with DNQX (10 to 20 μM) following which the membrane potential was depolarized to $+50\text{ mV}$ to record the corresponding NMDAR-mediated component of transmission (subsequently verified by pharmacological block with 100 μM dl-APV).

Field potential gamma oscillations

Midventral transverse hippocampal slices (350 μm) obtained as outlined above were immediately transferred to an interface-style chamber containing humidified carbogen gas and perfused at 32° to 34°C with aerated modified aCSF (1 to 1.5 ml/min) containing (in mM): 126 mM NaCl, 3 mM KCl, 2 mM MgCl₂, 2 mM CaCl₂, 1.25 mM NaH₂PO₄, 10 mM glucose, and 26 mM NaHCO₃. Slices were maintained for at least 1 hour after slicing before electrophysiological recordings were carried out. Local field potentials were recorded from hippocampal region CA3 in stratum pyramidale using glass pipettes pulled from standard borosilicate glass (3 to 5 megohm) filled with modified aCSF. Signals were low-pass-filtered at 2 kHz and captured using a Multiclamp 700B amplifier (Molecular Devices, CA), digitized using a Digidata 1322A (Molecular Devices, CA), and captured on a PC running pClamp 9 (Molecular Devices, CA). All data were imported into Igor Pro 6 (Wavemetrics, OR) using Neuromatic (ThinkRandom, UK) and analyzed using custom-written procedures. Persistent gamma oscillations were evoked by bath-applying carbachol at 25 μM for 30 min. Gamma oscillation power and frequencies were determined using power spectra derived from 300 s of recording, and analyses were carried out in a blinded manner. All data were tested for normality followed by

parametric or nonparametric analyses as appropriate in GraphPad Prism (GraphPad Software, CA).

RiboTag pulldown

Immunoprecipitation and purification of ribosome-associated RNA was performed from PV-Cre *k/+*; RiboTag *k/k* mouse brains as described (59) with minor modifications. Briefly, mouse cortex and hippocampus were homogenized in lysis buffer [50 mM tris, 100 mM KCl, 12 mM MgCl₂, 1% NP-40, cycloheximide (100 $\mu\text{g}/\text{ml}$), 10 mM ribonucleoside vanadyl complex, 1 mM dithiothreitol, plus RNasin and cOmplete EDTA-free protease inhibitor mixture (pH 7.4)] on ice. Homogenates were spun at 10,000g for 10 min to remove debris. Supernatant was collected, and ribosomes with associated RNA were immunoprecipitated by anti-HA antibody. Ribosome-associated RNA was purified by an RNeasy mini kit (Qiagen) and then subject to RNA-seq or qPCR as described in the “RNA Extraction, complementary DNA synthesis, and qPCR” section.

RNA-seq and data analysis

RNA-seq libraries were prepared using an Illumina TruSeq stranded RNA library preparation kit (catalog number: RS-122-2001, Illumina). Library quality was validated by high-sensitivity DNA analysis kit using Agilent Bioanalyzer 2100, and the concentration of RNA-seq libraries was quantified by qPCR using KAPA library quantification kit (Kapabiosystems).

Sequencing of RNA-seq libraries was performed on a HiSeq 2500 instrument (Illumina) with 100-base pair ($\times 2$) reads according to the manufacturer's instructions. Six libraries with distinct barcodes were sequenced in one lane. The depth of RNA-seq was $\sim 50 \times 10^6$ reads per sample. Paired-end RNA-seq reads were aligned to mouse genome GRCm38 using HISAT2 (60). Gene expression levels (FPKM) were obtained using StringTie (61). FPKM (fragments per kilobase of transcript per million mapped reads) values were \log_2 -transformed after adding a pseudo-count of one. Then, genes with \log_2 -transformed FPKM values less than 1 in all samples were filtered out, and the retained data were further quantile-normalized across samples. To identify genes that change between conditions [i.e., WT versus knockout (KO) and WT_SI versus KO_SI], we applied differential gene analysis using limma (62).

Pathway analysis

Pathway analysis was conducted using the Ingenuity Pathway Analysis platform (Qiagen) to determine pathways possibly affected by DEGs. For purposes of pathway analysis, those genes with differential \log_2 expression fold change of $>2\text{ SD}$ were deemed significant and compared to the full user transcript dataset to identify pathways of interest.

RNA extraction, complementary DNA synthesis, and qPCR

Total RNA was extracted by an RNeasy mini kit (Qiagen) according to the manufacturer's protocol. Isolated RNA was treated with deoxyribonuclease to remove DNA (Turbo DNA-free kit, Ambion). One microgram of isolated total RNA was then immediately reverse-transcribed into complementary DNA using the SuperScript First-Strand Synthesis System for reverse transcription PCR (Invitrogen). qPCR was performed with a QuantStudio 6 Flex system (Applied Biosystem) using SYBR green qPCR mastermix in a 384-well optical plate. PCR cycling consists of 95°C for 10 min, followed by 40 cycles of 95°C for 30 s, 60°C for 30 s, and 72°C for 30 s. A melt curve was conducted to determine the specificity of PCR amplification. *Gapdh* or *Sdha* served as an internal control to normalize data.

ROC curve analysis

To evaluate the diagnostic value of CSF biomarkers, ROC curve analysis was performed. ROC curve was created by plotting the true-positive rate (sensitivity) against the false-positive rate ($100 - \text{specificity}$) for different cutoff points. Each point on the ROC curve represented a sensitivity/specificity pair corresponding to a particular threshold. The area under the ROC curve indicated how well two diagnostic groups can be distinguished. Accuracy was defined as the proportion of true results in the whole population $[(\text{true-positive} + \text{true-negative})/(\text{true-positive} + \text{false-positive} + \text{true-negative} + \text{false-negative})]$. For each CSF biomarker, the cutoff point, which maximizes Youden index ($\text{sensitivity} + \text{specificity} - 1$), was selected to calculate the accuracy of a CSF biomarker as a diagnostic test.

Statistical analysis

We used GraphPad Prism version 9 (RRID: SCR_002798) to perform statistical analyses. Two-tailed *t* test was used to analyze difference between two groups. Correlation analysis were performed by Spearman's rank correlation coefficient. Sample sizes of human specimens were estimated by power analysis using G*Power (RRID: SCR_013726).

SUPPLEMENTARY MATERIALS

Supplementary material for this article is available at <https://science.org/doi/10.1126/sciadv.abf6935>

[View/request a protocol for this paper from Bio-protocol.](#)

REFERENCES AND NOTES

- M. J. Owen, A. Sawa, P. B. Mortensen, Schizophrenia. *Lancet* **388**, 86–97 (2016).
- F. J. Kallmann, The genetic theory of schizophrenia. *Am. J. Psychiatry* **103**, 309–322 (1946).
- M. Fromer, A. J. Pocklington, D. H. Kavanagh, H. J. Williams, S. Dwyer, P. Gormley, L. Georgieva, E. Rees, P. Palta, D. M. Ruderfer, N. Carrera, I. Humphreys, J. S. Johnson, P. Roussos, D. D. Barker, E. Banks, V. Milanova, S. G. Grant, E. Hannon, S. A. Rose, K. Chambert, M. Mahajan, E. M. Scolnick, J. L. Moran, G. Kirov, A. Palotie, S. A. McCarrroll, P. Holmans, P. Sklar, M. J. Owen, S. M. Purcell, M. C. O'Donovan, De novo mutations in schizophrenia implicate synaptic networks. *Nature* **506**, 179–184 (2014).
- Schizophrenia Working Group of the Psychiatric Genomics Consortium, Biological insights from 108 schizophrenia-associated genetic loci. *Nature* **511**, 421–427 (2014).
- E. C. Johnson, R. Border, W. E. Melroy-Greif, C. A. de Leeuw, M. A. Ehringer, M. C. Keller, No evidence that schizophrenia candidate genes are more associated with schizophrenia than noncandidate genes. *Biol. Psychiatry* **82**, 702–708 (2017).
- A. Sekar, A. R. Bialas, H. de Rivera, A. Davis, T. R. Hammond, N. Kamitaki, K. Tooley, J. Presumey, M. Baum, V. Van Doren, G. Genovese, S. A. Rose, R. E. Handsaker; Schizophrenia Working Group of the Psychiatric Genomics Consortium, M. J. Daly, M. C. Carroll, B. Stevens, S. A. McCarrroll, Schizophrenia risk from complex variation of complement component 4. *Nature* **530**, 177–183 (2016).
- R. Birnbaum, D. R. Weinberger, Genetic insights into the neurodevelopmental origins of schizophrenia. *Nat. Rev. Neurosci.* **18**, 727–740 (2017).
- G. Gonzalez-Burgos, D. A. Lewis, NMDA receptor hypofunction, parvalbumin-positive neurons, and cortical gamma oscillations in schizophrenia. *Schizophr. Bull.* **38**, 950–957 (2012).
- O. D. Howes, S. Kapur, The dopamine hypothesis of schizophrenia: Version III—the final common pathway. *Schizophr. Bull.* **35**, 549–562 (2009).
- J. T. Coyle, NMDA receptor and schizophrenia: A brief history. *Schizophr. Bull.* **38**, 920–926 (2012).
- A. Mohammadi, E. Rashidi, V. G. Amoeeian, Brain, blood, cerebrospinal fluid, and serum biomarkers in schizophrenia. *Psychiatry Res.* **265**, 25–38 (2018).
- A. Lanahan, G. Lyford, G. S. Stevenson, P. F. Worley, C. A. Barnes, Selective alteration of long-term potentiation-induced transcriptional response in hippocampus of aged, memory-impaired rats. *J. Neurosci.* **17**, 2876–2885 (1997).
- W. Zhang, J. Wu, M. D. Ward, S. Yang, Y. A. Chuang, M. Xiao, R. Li, D. J. Leahy, P. F. Worley, Structural basis of arc binding to synaptic proteins: Implications for cognitive disease. *Neuron* **86**, 490–500 (2015).
- W. Zhang, Y.-A. Chuang, Y. Na, Z. Ye, L. Yang, R. Lin, J. Zhou, J. Wu, J. Qiu, A. Savonenko, D. J. Leahy, R. Haganir, D. J. Linden, P. F. Worley, Arc oligomerization is regulated by CaMKII phosphorylation of the GAG domain: An essential mechanism for plasticity and memory formation. *Mol. Cell* **75**, 13–25.e5 (2019).
- J. D. Shepherd, G. Rumbaugh, J. Wu, S. Chowdhury, N. Plath, D. Kuhl, R. L. Haganir, P. F. Worley, Arc/Arg3.1 mediates homeostatic synaptic scaling of AMPA receptors. *Neuron* **52**, 475–484 (2006).
- S. Park, J. M. Park, S. Kim, J.-A. Kim, J. D. Shepherd, C. L. Smith-Hicks, S. Chowdhury, W. Kaufmann, D. Kuhl, A. G. Ryazanov, R. L. Haganir, D. J. Linden, P. F. Worley, Elongation factor 2 and fragile X mental retardation protein control the dynamic translation of Arc/Arg3.1 essential for mGluR-LTD. *Neuron* **59**, 70–83 (2008).
- M. Ren, V. Cao, Y. Ye, H. K. Manji, K. H. Wang, Arc regulates experience-dependent persistent firing patterns in frontal cortex. *J. Neurosci.* **34**, 6583–6595 (2014).
- V. Y. Cao, Y. Ye, S. Mastwal, M. Ren, M. Coon, Q. Liu, R. M. Costa, K. H. Wang, Motor learning consolidates Arc-expressing neuronal ensembles in secondary motor cortex. *Neuron* **86**, 1385–1392 (2015).
- F. Ango, L. Prézeau, T. Muller, J. C. Tu, B. Xiao, P. F. Worley, J. P. Pin, J. Bockaert, L. Fagni, Agonist-independent activation of metabotropic glutamate receptors by the intracellular protein Homer. *Nature* **411**, 962–965 (2001).
- J. H. Hu, J. M. Park, S. Park, B. Xiao, M. H. Dehoff, S. Kim, T. Hayashi, M. K. Schwarz, R. L. Haganir, P. H. Seeburg, D. J. Linden, P. F. Worley, Homeostatic scaling requires group I mGluR activation mediated by Homer1a. *Neuron* **68**, 1128–1142 (2010).
- G. H. Diering, R. S. Nirujogi, R. H. Roth, P. F. Worley, A. Pandey, R. L. Haganir, Homer1a drives homeostatic scaling-down of excitatory synapses during sleep. *Science* **355**, 511–515 (2017).
- J. M. Park, J. H. Hu, A. Milshteyn, P. W. Zhang, C. G. Moore, S. Park, M. C. Datko, R. D. Domingo, C. M. Reyes, X. J. Wang, F. A. Etzkorn, B. Xiao, K. K. Szumlinski, D. Kern, D. J. Linden, P. F. Worley, A prolyl-isomerase mediates dopamine-dependent plasticity and cocaine motor sensitization. *Cell* **154**, 637–650 (2013).
- M. C. Chang, J. M. Park, K. A. Pelkey, H. L. Grabenstatter, D. Xu, D. J. Linden, T. P. Sutula, C. J. McBain, P. F. Worley, Narp regulates homeostatic scaling of excitatory synapses on parvalbumin-expressing interneurons. *Nat. Neurosci.* **13**, 1090–1097 (2010).
- Y. Gu, S. Huang, M. C. Chang, P. Worley, A. Kirkwood, E. M. Quinlan, Obligatory role for the immediate early gene NARP in critical period Plasticity. *Neuron* **79**, 335–346 (2013).
- K. A. Pelkey, E. Barksdale, M. T. Craig, X. Yuan, M. Sukumaran, G. A. Vargish, R. M. Mitchell, M. S. Wyeth, R. S. Petralia, R. Chittajallu, R. M. Karlsson, H. A. Cameron, Y. Murata, M. T. Colonnese, P. F. Worley, C. J. McBain, Pentraxins coordinate excitatory synapse maturation and circuit integration of parvalbumin interneurons. *Neuron* **85**, 1257–1272 (2015).
- R. J. O'Brien, D. Xu, R. S. Petralia, O. Steward, R. L. Haganir, P. Worley, Synaptic clustering of AMPA receptors by the extracellular immediate-early gene product Narp. *Neuron* **23**, 309–323 (1999).
- D. Xu, C. Hopf, R. Reddy, R. W. Cho, L. Guo, A. Lanahan, R. S. Petralia, R. J. Wenthold, R. J. O'Brien, P. Worley, Narp and NP1 form heterocomplexes that function in developmental and activity-dependent synaptic plasticity. *Neuron* **39**, 513–528 (2003).
- R. W. Cho, J. M. Park, S. B. E. Wolff, D. Xu, C. Hopf, J. A. Kim, R. C. Reddy, R. S. Petralia, M. S. Perin, D. J. Linden, P. F. Worley, mGluR1/5-dependent long-term depression requires the regulated ectodomain cleavage of neuronal pentraxin NPR by TACE. *Neuron* **57**, 858–871 (2008).
- M. F. Xiao, D. Xu, M. T. Craig, K. A. Pelkey, C. C. Chien, Y. Shi, J. Zhang, S. Resnick, O. Pletnikova, D. Salmon, J. Brewer, S. Edland, J. Wegiel, B. Tycko, A. Savonenko, R. H. Reeves, J. C. Troncoso, C. J. McBain, D. Galasko, P. F. Worley, NPTX2 and cognitive dysfunction in Alzheimer's Disease. *eLife* **6**, e23798 (2017).
- M. Martineau, A. Somasundaram, J. B. Grimm, T. D. Gruber, D. Choquet, J. W. Taraska, L. D. Lavis, D. Perraes, Semisynthetic fluorescent pH sensors for imaging exocytosis and endocytosis. *Nat. Commun.* **8**, 1412 (2017).
- J. M. Coughlin, L. N. Hayes, T. Tanaka, M. Xiao, R. H. Yolken, P. Worley, F. M. Leweke, A. Sawa, Reduced superoxide dismutase-1 (SOD1) in cerebrospinal fluid of patients with early psychosis in association with clinical features. *Schizophr. Res.* **183**, 64–69 (2017).
- F. M. Leweke, A. Giffurda, D. Koethe, D. Schreiber, B. M. Nolden, L. Kranaster, M. A. Neatby, M. Schneider, C. W. Gerth, M. Hellmich, J. Klosterkötter, D. Piomelli, Anandamide levels in cerebrospinal fluid of first-episode schizophrenic patients: Impact of cannabis use. *Schizophr. Res.* **94**, 29–36 (2007).
- S. Kimoto, M. M. Zaki, H. H. Bazmi, D. A. Lewis, Altered markers of cortical γ -aminobutyric acid neuronal activity in schizophrenia. *JAMA Psychiat.* **72**, 747–756 (2015).
- G. G. Gross, J. A. Junge, R. J. Mora, H. B. Kwon, C. A. Olson, T. T. Takahashi, E. R. Liman, G. C. R. Ellis-Davies, A. W. McGee, B. L. Sabatini, R. W. Roberts, D. B. Arnold, Recombinant probes for visualizing endogenous synaptic proteins in living neurons. *Neuron* **78**, 971–985 (2013).
- H. M. Van't Spijker, D. Rowlands, J. Rossier, B. Haenzi, J. W. Fawcett, J. C. F. Kwok, Neuronal pentraxin 2 binds PNNs and enhances PNN formation. *Neural Plast.* **2019**, 6804575 (2019).

36. M. Ai, H. Mills, M. Kanai, J. Lai, J. Deng, E. Schreiter, L. Looger, T. Neubert, G. Suh, Green-to-Red Photoconversion of GCaMP. *PLoS ONE* **10**, e0138127 (2015).
37. D. Severin, S. Z. Hong, S.-E. Roh, S. Huang, J. Zhou, M. C. D. Bridi, I. Hong, S. Murase, S. Robertson, R. P. Haberman, R. L. Huganir, M. Gallagher, E. M. Quinlan, P. Worley, A. Kirkwood, All-or-none disconnection of pyramidal inputs onto parvalbumin-positive interneurons gates ocular dominance plasticity. *Proc. Natl. Acad. Sci. U.S.A.* **118**, e2105388118 (2021).
38. B. P. Lucey, T. J. Hicks, J. S. McLeland, C. D. Toedebusch, J. Boyd, D. L. Elbert, B. W. Patterson, J. Baty, J. C. Morris, V. Ovod, K. G. Mawuenyega, R. J. Bateman, Effect of sleep on overnight cerebrospinal fluid amyloid β kinetics. *Ann. Neurol.* **83**, 197–204 (2018).
39. J. K. Holth, S. K. Fritsch, C. Wang, N. P. Pedersen, J. R. Cirrito, T. E. Mahan, M. B. Finn, M. Manis, J. C. Geerling, P. M. Fuller, B. P. Lucey, D. M. Holtzman, The sleep-wake cycle regulates brain interstitial fluid tau in mice and CSF tau in humans. *Science* **363**, 880–884 (2019).
40. N. R. Barthelemy, H. Liu, W. Lu, P. T. Kotzbauer, R. J. Bateman, B. P. Lucey, Sleep deprivation affects Tau phosphorylation in human cerebrospinal fluid. *Ann. Neurol.* **87**, 700–709 (2020).
41. K. B. Hengen, M. E. Lambo, S. D. Van Hooser, D. B. Katz, G. G. Turrigiano, Firing rate homeostasis in visual cortex of freely behaving rodents. *Neuron* **80**, 335–342 (2013).
42. V. V. Vyazovskiy, C. Cirelli, M. Pfister-Genskow, U. Faraguna, G. Tononi, Molecular and electrophysiological evidence for net synaptic potentiation in wake and depression in sleep. *Nat. Neurosci.* **11**, 200–208 (2008).
43. L. de Vivo, M. Bellesi, W. Marshall, E. A. Bushong, M. H. Ellisman, G. Tononi, C. Cirelli, Ultrastructural evidence for synaptic scaling across the wake/sleep cycle. *Science* **355**, 507–510 (2017).
44. F. Manago, M. Mereu, S. Mastwal, R. Mastrogiacomo, D. Scheggia, M. Emanuele, M. A. De Luca, D. R. Weinberger, K. H. Wang, F. Papaleo, Genetic disruption of Arc/Arg3.1 in mice causes alterations in dopamine and neurobehavioral phenotypes related to schizophrenia. *Cell Rep.* **16**, 2116–2128 (2016).
45. A. M. Blouin, S. Han, A. M. Pearce, K. Cheng, J. J. Lee, A. W. Johnson, C. Wang, M. J. During, P. C. Holland, Y. Shaham, J. M. Baraban, I. M. Reti, Role of medial prefrontal cortex Narp in the extinction of morphine conditioned place preference. *Learn. Mem.* **20**, 75–79 (2013).
46. M. Niwa, R. S. Lee, T. Tanaka, K. Okada, S. I. Kano, A. Sawa, A critical period of vulnerability to adolescent stress: Epigenetic mediators in mesocortical dopaminergic neurons. *Hum. Mol. Genet.* **25**, 1370–1381 (2016).
47. A. Ieraci, A. Mallei, M. Popoli, Social isolation stress induces anxious-depressive-like behavior and alterations of neuroplasticity-related genes in adult male mice. *Neural Plast.* **2016**, 1–13 (2016).
48. G. Buzsaki, N. Logothetis, W. Singer, Scaling brain size, keeping timing: Evolutionary preservation of brain rhythms. *Neuron* **80**, 751–764 (2013).
49. T. Soda, C. Frank, K. Ishizuka, A. Baccarella, Y. U. Park, Z. Flood, S. K. Park, A. Sawa, L. H. Tsai, DISC1-ATF4 transcriptional repression complex: Dual regulation of the cAMP-PDE4 cascade by DISC1. *Mol. Psychiatry* **18**, 898–908 (2013).
50. S. Tsugawa, Y. Noda, R. Tarumi, Y. Mimura, K. Yoshida, Y. Iwata, M. Elsalhy, M. Kuromiya, S. Kurose, F. Masuda, S. Morita, K. Ogyu, E. Plitman, M. Wada, T. Miyazaki, A. Graff-Guerrero, M. Mimura, S. Nakajima, Glutathione levels and activities of glutathione metabolism enzymes in patients with schizophrenia: A systematic review and meta-analysis. *J. Psychopharmacol.* **33**, 1199–1214 (2019).
51. Z. Ma, G. G. Turrigiano, R. Wessel, K. B. Hengen, Cortical circuit dynamics are homeostatically tuned to criticality in vivo. *Neuron* **104**, 655–664 e4 (2019).
52. K. Wulff, D. J. Dijk, B. Middleton, R. G. Foster, E. M. Joyce, Sleep and circadian rhythm disruption in schizophrenia. *Br. J. Psychiatry* **200**, 308–316 (2012).
53. J. Wu, R. S. Petralia, H. Kurushima, H. Patel, M.-y. Jung, L. Volk, S. Chowdhury, J. D. Shepherd, M. Dehoff, Y. Li, D. Kuhl, R. L. Huganir, D. L. Price, R. Scannevin, J. C. Troncoso, P. C. Wong, P. F. Worley, Arc/Arg3.1 regulates an endosomal pathway essential for activity-dependent beta-amyloid generation. *Cell* **147**, 615–628 (2011).
54. T. Keck, T. Toyozumi, L. Chen, B. Doiron, D. E. Feldman, K. Fox, W. Gerstner, P. G. Haydon, M. Hübener, H. K. Lee, J. E. Lisman, T. Rose, F. Sengpiel, D. Stellwagen, M. P. Stryker, G. G. Turrigiano, M. C. van Rossum, Integrating Hebbian and homeostatic plasticity: The current state of the field and future research directions. *Philos. Trans. R. Soc. Lond. B Biol. Sci.* **372**, 20160158 (2017).
55. I. E. Sommer, C. E. Bearden, E. van Dellen, E. J. Breetvelt, S. N. Duijff, K. Majjer, T. van Amelsvoort, L. de Haan, R. E. Gur, C. Arango, C. M. Díaz-Caneja, C. H. Vinkers, J. A. S. Vorstman, Early interventions in risk groups for schizophrenia: What are we waiting for? *NPJ Schizophr.* **2**, 16003 (2016).
56. M. Watanabe, K. Nakano, H. Matsunari, T. Matsuda, M. Maehara, T. Kanai, M. Kobayashi, Y. Matsumura, R. Sakai, M. Kuramoto, G. Hayashida, Y. Asano, S. Takayanagi, Y. Arai, K. Umeyama, M. Nagaya, Y. Hanazono, H. Nagashima, Generation of interleukin-2 receptor gamma gene knockout pigs from somatic cells genetically modified by zinc finger nuclease-encoding mRNA. *PLoS ONE* **8**, e76478 (2013).
57. A. Parslow, A. Cardona, R. J. Bryson-Richardson, Sample drift correction following 4D confocal time-lapse imaging. *J. Vis. Exp.* 51086 (2014).
58. K. D. LaClair, K. F. Manaye, D. L. Lee, J. S. Allard, A. V. Savonenko, J. C. Troncoso, P. C. Wong, Treatment with bexarotene, a compound that increases apolipoprotein-E, provides no cognitive benefit in mutant APP/PS1 mice. *Mol. Neurodegener.* **8**, 18 (2013).
59. E. Sanz, L. Yang, T. Su, D. R. Morris, G. S. McKnight, P. S. Amieux, Cell-type-specific isolation of ribosome-associated mRNA from complex tissues. *Proc. Natl. Acad. Sci. U.S.A.* **106**, 13939–13944 (2009).
60. D. Kim, B. Langmead, S. L. Salzberg, HISAT: A fast spliced aligner with low memory requirements. *Nat. Methods* **12**, 357–360 (2015).
61. M. Perte, G. M. Perte, C. M. Antonescu, T. C. Chang, J. T. Mendell, S. L. Salzberg, StringTie enables improved reconstruction of a transcriptome from RNA-seq reads. *Nat. Biotechnol.* **33**, 290–295 (2015).
62. M. E. Ritchie, B. Phipson, D. Wu, Y. Hu, C. W. Law, W. Shi, G. K. Smyth, *limma* powers differential expression analyses for RNA-sequencing and microarray studies. *Nucleic Acids Res.* **43**, e47 (2015).

Acknowledgments: We thank D. Weinberger and the Lieber Institute for access to human brain tissue and helpful discussions. **Funding:** This work was supported by R35NS097966 to P.F.W.; NIH National Center for Advancing Translational Sciences (UL1 TR000448 and KL2 TR000450), NIH National Institute on Aging (R03 AG047999, K76 AG054863, P50 AG05681, and P01 AG26276), and McDonnell Center for Systems Neuroscience at Washington University School of Medicine to B.P.L.; MH-094268, Silvio O. Conte Centre and MH-092443, MH-105660, MH-107730, and S&R/RUSK, the Stanley Foundation to A. Sawa and L.N.H.; R01NS-081678 to D.B.A.; NIA RF1 A055974 to A. Sav.; the Stanley Foundation to F.M.L.; and an NICHD intramural research award to C.J.M., K.A.P., and M.T.C. **Author contributions:** M.-F.X., C.-C.C., and D.X. performed human CSF and postmortem brain studies. S.-E.R., J.Z., and M.J. constructed AAV2-CaMKII-NPTX2-SEP and AAV2-CaMKII-NPTX2-HA-V5 and performed two-photon microscopy experiments. M.-F.X. and C.-C.C. performed RiboTag and RNA-seq experiments. B.P.L. collected sleep intervention CSF. L.N.H., J.M.C., and F.M.L. collected schizophrenia CSF. W.Z. and C.C.T.J. analyzed RNA-seq data. M.T.C. and K.A.P. performed electrophysiology recording and analyses. M.S., C.J., I.M.R., and A. Sav. performed mouse behavior experiments. D.B.A. generated AAV-Flex-PSD95.FingR-tdTomato construct. P.F.W. directed and supervised this project. P.F.W., M.-F.X., and S.-E.R. prepared the manuscript with input from A. Saw., L.N.H., B.P.L., D.B.A., K.A.P., C.J.M., and A. Sav. **Competing interests:** P.F.W., D.X., and M.-F.X. are cofounders of CogNext. P.F.W., D.X., and M.-F.X. are inventors on patents related to this work filed by Johns Hopkins University (no. US10222386B2, filed 18 September 2015, published 5 March 2019 and no. US10914749B2, filed 1 February 2019, published 9 February 2021). All authors declare that they have no other competing interests. **Data and materials availability:** RNA-seq data were deposited in Gene Expression Omnibus (GEO: GSE150671). The CSF samples can be provided by Central Institute of Mental Health, Heidelberg University, pending scientific review and a completed material transfer agreement. Requests for the CSF samples should be submitted to F.M.L. All other data needed to evaluate the conclusions in the paper are present in the paper and/or the Supplementary Materials.

Submitted 12 November 2020

Accepted 5 October 2021

Published 24 November 2021

10.1126/sciadv.abf6935

A biomarker-authenticated model of schizophrenia implicating NPTX2 loss of function

Mei-Fang XiaoSeung-Eon RohJiechao ZhouChun-Che ChienBrendan P. LuceyMichael T. CraigLindsay N. HayesJennifer M. CoughlinF. Markus LewekeMin JiaDesheng XuWeiqiang ZhouC. Conover Talbot Jr.Don B. ArnoldMelissa StaleyCindy JiangIrving M. RetiAkira SawaKenneth A. PelkeyChris J. McBainAlena SavonenkoPaul F. Worley

Sci. Adv., 7 (48), eabf6935. • DOI: 10.1126/sciadv.abf6935

View the article online

<https://www.science.org/doi/10.1126/sciadv.abf6935>

Permissions

<https://www.science.org/help/reprints-and-permissions>

Use of think article is subject to the [Terms of service](#)

Science Advances (ISSN) is published by the American Association for the Advancement of Science. 1200 New York Avenue NW, Washington, DC 20005. The title *Science Advances* is a registered trademark of AAAS.

Copyright © 2021 The Authors, some rights reserved; exclusive licensee American Association for the Advancement of Science. No claim to original U.S. Government Works. Distributed under a Creative Commons Attribution NonCommercial License 4.0 (CC BY-NC).